Louise M. Vick · Martina Böhme · Line Rouyet · Steffen G. Bergh · Geoffrey D. Corner · Tom Rune Lauknes

Structurally controlled rock slope deformation in northern Norway

Abstract Gravitational forcing of oversteepened rock mass leads to progressive failure, including rupture, creeping, sliding and eventual avalanching of the unstable mass. As the point of rupture initiation typically follows pre-existing structural discontinuities within the rock mass, understanding the structural setting of slopes is necessary for an accurate characterisation of the hazards and estimation of the risk to life and infrastructure. Northern Norway is an alpine region with a high frequency of large rock slope deformations. Inherited structures in the metamorphic bedrock create a recurring pattern of anisotropy, that, given certain valley orientations, causes mass instability. We review the geomorphology, structural mechanics and kinematics of nine deforming rock slopes in Troms County, with the aim of linking styles of deformation. The limits of the unstable rock mass follow either foliation planes, joint planes or inherited faults, depending on the valley aspect, slope angle, foliation dip and proximity to fault structures. We present an updated geotechnical model of the different failure mechanisms, based on the interpretations at each site of the review.

Introduction

Catastrophic failure of rock slope deformations (after Hungr et al. 2014, herein RSD) is a serious hazard in mountainous Norway (Blikra et al. 2006b; Furseth 2006; Hermanns and Longva 2012). More than 130 RSDs are identified in the Troms region of northern Norway (NGU 2019a). Slope failures resulting in landslides, displacement wave generation and landslide dams pose a severe threat to the local population. For these sites, accurate structural characterisation of the slope is necessary to quantify the volumes, characterise the hazard and estimate the risk to life and infrastructure. Many of the RSDs in Troms have been the focus of field campaigns (e.g. Bunkholt et al. 2011, 2013a, b; Hannus 2011; Eriksen et al. 2017a, b) and reviews (Bunkholt et al. 2012, 2013a, b). It is understood that the behaviour of RSDs is largely controlled by pre-existing bedrock structure (Cruden and Varnes 1996; Agliardi et al. 2001; Glastonbury and Fell 2010; Jaboyedoff et al. 2009; Humair et al. 2013; Stead and Wolter 2015; Pedrazzini et al. 2016) and understanding the dominant controlling structures of an unstable slope increases the accuracy of volume and runout predictions of failure scenarios (Oppikofer et al. 2016). Local structural and geomorphological studies combined with measurements of displacement provide a frame to discuss initiation, deformation and movement processes for various types of RSD in Troms (Lauknes et al. 2010; Henderson et al. 2011; Böhme et al. 2016b, 2019; Eriksen 2017; Eriksen et al. 2017a, b). However, the characterisation of these slopes is complicated by complex deformation morphology, multiple failure mechanisms, ongoing rockfall and superficial and periglacial processes. This activity obscures

diagnostic morphostructure. Despite the cluster of RSDs recognised in Troms (NGU 2019a), limited studies are published which postulate failure mechanisms of the slope deformations (e.g. Böhme et al. 2016b; Eriksen et al. 2017b). Studies linking failure mechanism to inherited bedrock structure typically focus on southwestern parts of Norway (Henderson and Saintot 2011; Saintot et al. 2011; Penna et al. 2017) but are limited in the north (Braathen et al. 2004; Bunkholt et al. 2013b).

In this article, we review the morphology, internal structure and movement rates of nine rockslides on the sides of steep glacial valleys and fjords in Troms in order to exemplify various types of RSDs in the region and to explore the relationship between slope instability and bedrock structure. The review intends to provide a background on past and ongoing work on structurally controlled rock slope failures and mechanisms in northern Norway.

Data

We interpret morphostructure and failure mechanisms based on a 0.5-m resolution aerial laser scanning (ALS) digital elevation model (DEM) (Kartverket 2019a), geological maps (Zwaan 1988; Zwaan et al. 1998, 2006; Quenardel and Zwaan 2008) and extensive data sets (Nordvik et al. 2010; Husby 2011; Rasmussen 2011; Hannus 2012; Bunkholt et al. 2012, 2013a, b; Blikra and Christiansen 2014; Böhme et al. 2016a, 2019; Bredal 2016; Eriksen et al. 2017b; Eriksen 2017; Eriksen et al. 2017a; Andresen 2018) including field data collected sporadically by the authors from 1969 and intensely from 2008. We compared the structural setting to kinematic information using (1) in situ differential Global Navigation Satellite Systems (dGNSS) measurements when available and (2) synthetic aperture radar interferometry (InSAR) measurements based on 2015–2018 Sentinel-1 satellite images (free and open InSAR Norway mapping service insar.no; NGU 2019b) processed with a persistent scatterer interferometry algorithm (Ferretti et al. 2000, 2001). It should be noted that InSAR maps shown in the "Conceptual model and categories of structurally controlled RSDs" section document ground surface mean velocities without any information about the deformation mechanism and must thus be interpreted carefully in the context of each specific study site. InSAR measurements are one-dimensional and correspond to changes in sensor-ground distance, i.e. displacement along the radar line-of-sight (LOS), depending on the satellite acquisition geometry. Areas without any InSAR information do not correspond to stable parts but to areas where no displacement information can be retrieved due to geometrical effects or decorrelation due to vegetation, snow, wet or quickly changing surfaces. For more information about the potential and limitations of InSAR for the characterisation of RSDs, see Barboux et al. (2015), Carlà et al. (2019), Eriksen et al. (2017a), Frattini et al. (2018), Lauknes et al. (2010) and Schlögel et al. (2016).

Study area

The topography of Troms is largely alpine, formed over more than 20 glacial cycles in the Scandinavian Mountains (Corner 2005). The region has a wide coastal margin dissected by fjords and valleys delineating high peaks (< 1800 m asl). Inland the terrain is flat topped (< 1000 m asl) with palaeo surfaces delineated by river valleys. The slopes considered in this study are predominantly creeping rockslides (Radbruch-Hall 1978; Chigira 1992) and deep-seated gravitational slope deformations (DSGSD; Agliardi et al. 2001; Pánek and Klimeš 2016). They tend to form on valley and fjord flanks where mountains often display plateau morphology of relict surfaces (Schermer et al. 2017). Most of the RSDs exist within, or at the transition from, the coastal margin to the inland plateaus, with an obvious cluster at the transition in central Troms (Fig. 1; Blikra et al. 2006b). The unstable areas are situated on moderate to steep (ca 20–35°) and high (ca 800–1200 m) slopes. The RSDs are easily identified by obvious slope morphostructure, including sharp back and lateral scarps, translated rock blocks forming terraces, locally highly fractured rock, increased talus cover, toe buckling and deposit lobes from previous rock avalanche events.

The study area lies within the subarctic climate zone, characterised by long cold winters and short cool summers. Annual precipitation can range from 500 to slightly over 1000 mm, with a wetter, milder climate in the coastal margin (eKlima 2020). The snow cover may be preserved as long as 8 months, with significant melting occurring between May and June (Blikra and Christiansen 2014).

Deglaciation of the fjords in the map area (Fig. 1) occurred between 11 (western margin) and 9.7 ka (eastern margin; icemap.no; Patton et al. 2017). Subsequent paraglacial processes have reshaped the landscape (Ballantyne 2002; Jarman 2009). Extensive dating records across Norway indicate an instability response in rock slopes following ice retreat and again during the Holocene climate optimum. From then, landslide activity has remained consistent (Hermanns et al. 2017). The cluster of identified rock glaciers in the area (Lilleøren and Etzelmüller 2011) illustrates the cryo-conditioning of the landscape evolution (Berthling and Etzelmüller 2011). Exposure dating of the backscarp of an active RSD in this study (Gámanjunni-3) suggests displacement initiated between 6.6 and 4.3 ka (Böhme et al. 2019), indicating that rockslides in the area have a long deformation history conditioned by Holocene climatic events. Peaks in Holocene landslide activity have also been attributed to periods of seismic activity due to isostatic uplift (Bøe et al. 2004). The Baltic Shield is generally thought to be aseismic; however, some evidence of neotectonics have been reported in northern Norway. Associated earthquakes could trigger mass slope failure in the region (Olesen et al. 2004, 2013).

The bedrock of Troms is dominated by Caledonian nappes of the Upper Allochthon (Andresen, 1985), with basement rocks of the Fennoscandian Shield outcropping in erosion windows and in coastal areas (Zwaan 1988; Bergh et al., 2007). Rocks of the thrust nappes were all metamorphosed, stacked, imbricated and folded during multiple events, on all scales, resulting in a complex fold-thrust belt architecture (Augland et al. 2014). Major and minor thrusts, ductile shear zones and foliation/cleavage all dip dominantly to the NW, aligning with this nappe-imbricate phenomenon (Gee et al. 2008; Augland et al. 2014). The medium- to high-grade metamorphic rocks span lithologies from meta-arkose to the ultramafic, the dominant lithologies being mica schists and gabbros (Zwaan 1988). RSDs are distributed throughout the different rock types, but show a higher density within the mica schists (Blikra et al. 2006b; Bunkholt et al. 2012).

Major rift-related offshore and onshore faults and smaller-scale discontinuities within the fault damage zone align with one another (Roberts and Lippard 2005; Bergh et al. 2007; Indrevær et al. 2013, 2014; Davids et al. 2013; Koehl 2018; Fig. 3). These structures are characterised by rhombic, zigzag-shaped structures (in map view) striking variably NNE–SSW, NE–SW and NW–SE (Bergh et al. 2007; Eig 2008; Eig and Bergh 2011; Hansen and Bergh 2012; Indrevær et al. 2013). Most mapped onshore structures display steep to near-vertical dip angles, i.e. rarely dip < 60°, while low-angle structures (listric extensional fault geometries) occur at greater depth in the crust (Indrevær et al. 2013, 2014).

Conceptual model and categories of structurally controlled RSDs

In order to interpret the complex subsurface geometries, we consider all RSDs in this study as compound slide types (after Glastonbury and Fell (2010) and Hungr et al. (2014)), defined as rockslides with rupture surfaces following one or more planar structure, and which typically exhibit both tensile damage at the head and compressive damage at the toe. We apply the progressive model of failure (Fig. 2), which describes the process from the onset of slope damage, the accumulation of slope damage to catastrophic failure (e.g. Dick et al. 2015; Sullivan 2007; Stead et al. 2007; 'catastrophic failure' after Hermanns and Longva 2012). From the onset of the progressive failure process, surface rupture within the slope occurs (Yerro et al. 2016). The rupture surfaces propagate through the rock mass by combining both pre-existing discontinuities and new fractures formed by the breakage of rock bridges (step fractures) until it is kinematically feasible for the mass to fail (Stead and Eberhardt 2013). We simplify the bounding rupture surfaces of the rockslide as the *rear rupture surface* and *basal rupture surface*, the planes that delineate the upper and lower portions of the rockslide (Glastonbury and Fell 2010).

The RSDs have been categorised, for presentation purposes, into which pre-existing structures are utilised for the rear rupture of the slide. We propose that the specific structure utilised depends on foliation orientation at the slope and the presence of faults (Fig. 3). We therefore present three categories. Where foliation dips moderately to steeply with the slope, foliation sliding is feasible and the rear rupture surface is comprised of foliation planes. We term this 'foliation-controlled rear rupture'. Where it is shallow dipping, dipping into the slope or obliquely to the slope, foliation sliding is not feasible, and other failure mechanisms must be employed, such a rupture utilising steep joint planes. We term this 'joint-controlled rear rupture'. Where a fault is present, it presents a major structural weakness and forms the rear rupture surface. We term this 'fault-controlled rear rupture'. In this study, all fault plane rupture sites have shallow-dipping foliation, and the question of foliation dominance at sites where foliation may be steep will be therefore discussed in a separate section.

We review three mapped sites in each category. Foliation-controlled rear rupture RSDs discussed here include Nomedalstinden, Rismmalčohkka and Badjánanvárri (Fig. 1). Other examples in the mapping area include parts of Gavtavarri
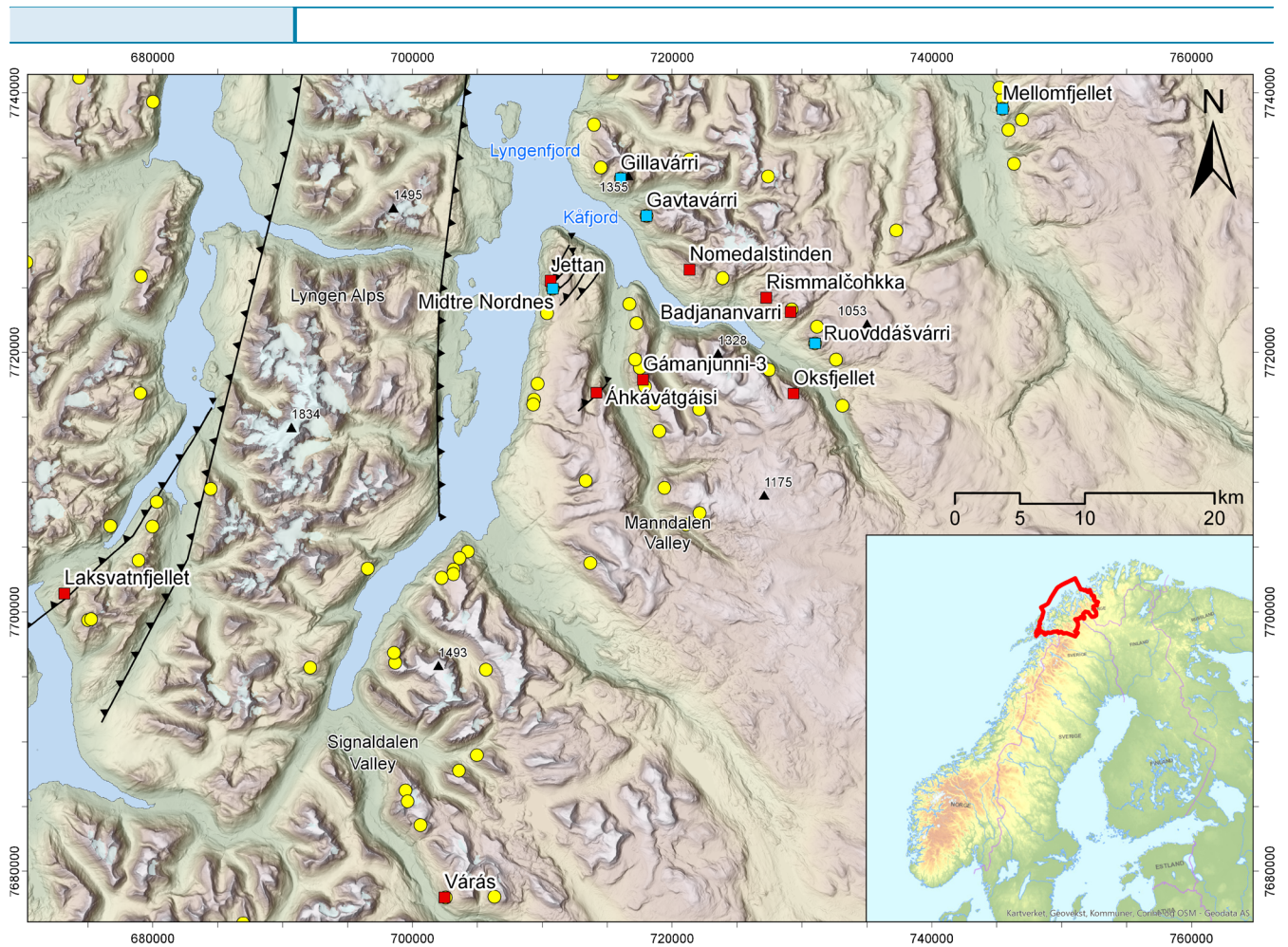
Fig. 1 Relief map of central Troms. Map displays the location of mapped RSDs (yellow dots, NGU 2019a), sites discussed in this contribution (red squares) and other sites mentioned (blue squares). Faults presented here are only those discussed in this paper. The Lyngen Fault complex borders the Lyngen Alps (after Osmundsen et al. 2009), the Laksvatn Fault goes through Balsfjord and towards the western Lyngen Fault (after Davids et al. 2013) and the fault traces across Laksvatnfjellet and at Áhkávátgáisi (Bunkholt et al. 2013b). Inset shows the location of Troms County (red polygon) in Norway. Grid in UTM33

(Andresen 2018) and Giilavarri (Bunkholt et al. 2011). Joint-controlled rear rupture examples discussed here include Gámanjunni-3, Váráš and Oksfjellet. However, many other examples exist in the mapping area which fit this category, e.g. Midtre Nordnes (Hernes 2014), Ruovddášvárri (Andresen 2018) and Mellomfjellet (Sikveland 2019). Fault-controlled rear rupture RSDs discussed here include Jettan, Laksvatnfjellet and Áhkávátgáisi. Other examples in the mapping area have not yet been identified.

Foliation-controlled rear rupture
The three sites discussed in this category are found in the Kåfjord valley (Fig. 1). The valley aligns NW–SE, with a local foliation dip measured at the head of the mountains between 30 and 40° to SW, making the northern flank of the fjord ideal for foliation-controlled rear rupture.

Nomedalstinden
Nomedalstinden (Figs. 4 and 5) rises 1051 m above the fjord, as well as houses and infrastructure. The unstable area consists of meta-

arkose/quartzite, mica schists and banded gneiss (Zwaan et al. 2006). The foliation dips SW at an average of 32° at the head of the slope at shallows to an average of 15° towards the fjord. The mountain slope falls at an average of 20°, characterised by an undulating surface with rounded morphostructure and a high mass of talus leading to the formation of a large rock glacier complex (Tolgensbakk and Sollid 1988). Nomedalstinden has classic deep-seated gravitational slope deformation (DSGSD) morphology (Agliardi et al. 2001). Following the ridge of the mountain is a large (ca 1.5 km-long) foliation-parallel backscarp (dipping SW to WSW), immediately succeeded by a counterscarp, together forming a double-crested ridgeline (Fig. 5, Husby 2011; Andresen 2018). These exposed surfaces display evidence of intense shearing with slickenlines and mineral alteration (Fig. 6 c and d). Below the double-crested ridgeline is a series of parallel scarps also formed by foliation sliding (Fig. 5). Scarps delineate dislocated terraces which often display a preserved surface. Terraces are crosscut by open fractures utilising joint sets dipping steeply (75–80°) and striking E–W, NE–SW and NW–SE. They indicate a lateral spread component to the sliding (Husby 2011).
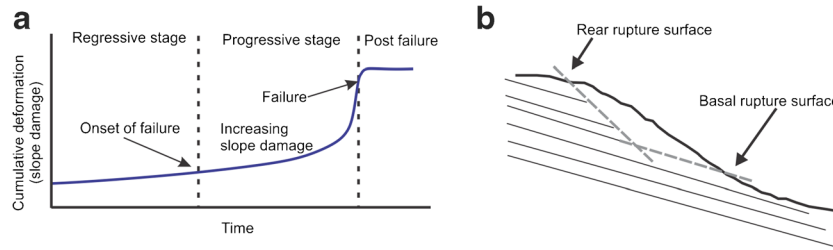
Fig. 2 **a** Stages of slope failure modified after Stead and Eberhardt (2013) and Dick et al. (2015). The onset of failure occurs at the transition between the regressive and progressive stages at which time the rate of damage increases in the rock slope. **b** A compound rockslide model indicating the rear and basal rupture surface as the major bounding structures of a rockslide. Modified after Glastonbury and Fell (2010)

Through the central section of the unstable area, the morpho-structure is obscured by several rock glacier units, their presence indicating a supply of material from localised rock avalanche and rockfall events in the upper portion of the RSD. The lower portion of the slope contains some minor scarps, frequent open surface fractures, localised rockfalls and groundwater seepage. The toe of this slide is interpreted from buckling observed in the slope morphology and by following the clear line of the back scarp at the SE side downwards. Small streams seeping from the toe 'line' confirm that a dominant structure daylights here, and surface cracking and rockfall activity indicates localised deformation taking place, evidence that compression is taking place. A compound slide mechanism is proposed, where the rupture surface follows steep foliation at the rear and shallow foliation at the base. Projecting the uppermost rupture surface to the inferred toe point indicates a transfer in the centre of the RSD to allow for load transfer from rear to base. This may be accommodated by low-angle step fractures, or locally varied foliation which cannot been mapped at the surface due to surficial material coverage (Fig. 5).

The InSAR LOS orientation is close to perpendicular to the slope aspect (black arrow, Fig. 4b), not ideal for capturing SW horizontal movement. However, some of the vertical and westward horizontal components of the movement can be detected. There is not a coherent pattern of movement across the slope, with background values showing low amounts of movement (< 2.5 mm a^{-1} along LOS). In the NW, the upper part of large rock glaciers show the highest movement (> 30 mm a^{-1} along LOS). Moderate amounts of movement align with the steep front of the dislocated terraces in the upper and central area (5–15 mm a^{-1} along LOS), likely indicating surficial displacement of the colluvium. A lack of consistent surface movement across the site may imply that either (1) the RSD is in an early phase of development and the degree of slope damage has not progressed to the point where the mass can slide, or (2) the RSD is 'locked up' at the toe, becoming dormant (after Cruden and Varnes 1996) after reaching equilibrium.

Rismmalčohkka

Rismmalčohkka (Figs. 7, 8 and 9), 6 km SE of Nomedalstinden, lies adjacent to the mouth of Kåfjord and above the village of Trollvik. The mountain comprises meta-arkose/quartzite, mica schists and banded gneiss (Zwaan et al. 2006). It slopes from a striking backscarp ridgeline traced across the peak at 1096 m asl gently down to fjord level at an average of 20°. The scarp curves from a SW dip at the eastern end, to a S dip at the western end. It is dominantly foliation-parallel, dipping 30–35° and is up to 100 m

high and 1.5 km long (Figs. 8 and 9a). The rupture surface contains downslope movement indicators and is heavily oxidised.

The upper portion of the mountain displays a hummocky sagging morphology, with numerous foliation-parallel scarps up to 100 m high segmenting terraces (Figs. 7 and 8). The terrace surfaces display evidence of lateral spreading, with surfaces cross-cut by slight transverse depressions. Talus covers the upper half of the mountain, indicating ongoing superficial and periglacial processes. The talus supplies several rock glaciers framing the RSD (Tolgensbakk and Sollid 1988). The transition from talus cover to vegetated slope in the central slope is marked by ca 50 m wide graben structures striking NW–SE (Fig. 9c). The transition also marks a change in foliation dip to an average of 30° W.

The NW end of the grabens delimits a bedrock knob below, the graben indicating slight dislocation of the knob has occurred. Slope damage is accumulating within the knob, evidenced by its fractured surface and small avalanche scars (Fig. 7a). In the lower SE section of the mountain, the terrain is smoothed, with glacial geomorphic features present including moraines and meltwater channels (Tolgensbakk and Sollid 1988). Some of the glacial features are dissected by morphostructure, confirming post-glacial deformation.

No clear toe has been mapped; however, some surface fracturing is apparent in the bedrock of the lower slope, and a slope break indicates that the surface is buckled (Figs. 7 and 8). The toe line has been inferred at the slope break and delimits the extent of observable deformation (Figs. 7 and 9d). It is possible that the basal rupture surface daylights in the fjord basin, or possible there is no clear toe at all, a diagnostic characteristic of DSGSD (Agliardi et al. 2012). The foliation shallows towards the inferred toe with respect to the slope direction (16° apparent dip in cross section A–A', Fig. 8). Therefore, the rear rupture surface likely transitions to a basal rupture surface which follows the foliation (as mapped at the scarp) and some low-angled step fractures to achieve daylighting in the surface at the toe. A toe line has been inferred which divides rough hummocky terrain from smoothed flatter terrain near the fjord; however, no clear indications of a daylighting toe have been mapped.

As for Nomedalstinden, the InSAR LOS is not ideal for capture of SW horizontal movement (black arrow, Fig. 7b). However, areas affected by horizontal westward and vertical components of movement can be highlighted. The central upper part of the slope shows a homogeneous pattern of low velocities (2.5–15 mm a^{-1} along LOS). The upper terraces show higher velocities (15–20 mm a^{-1} along LOS). The moving areas align with the mapped structures;
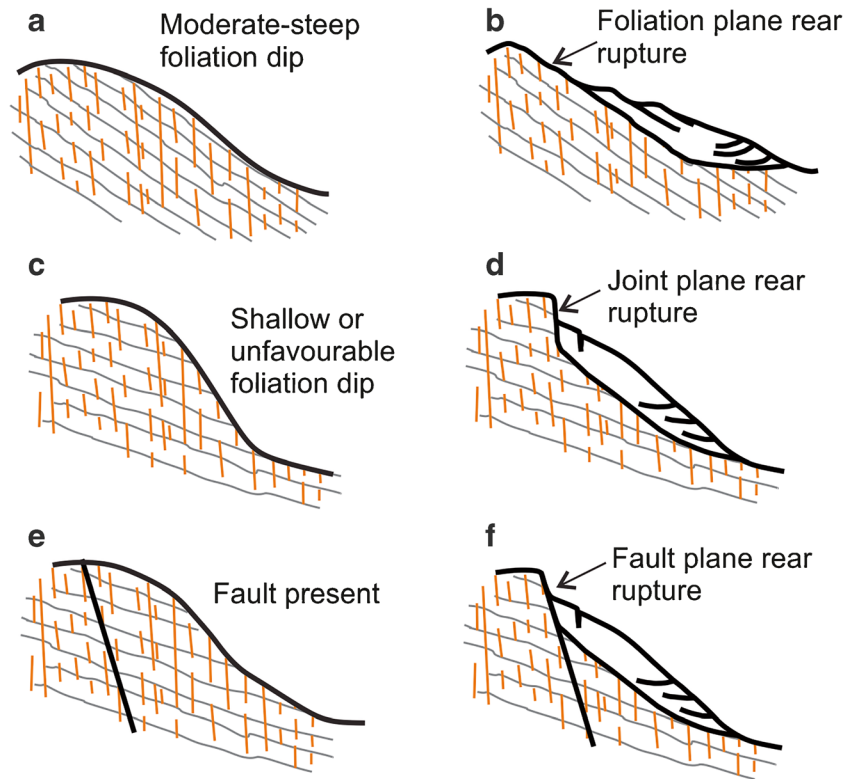
Fig. 3 Schematic overview of foliation orientations and subsequent failure mechanisms. At all sites, joint sets are vertical to subvertical, but foliation varies. **a** Foliation dips moderately to steeply with the slope, this allows kinematically for foliation-parallel sliding at the head of the slope (**b**). In scenario **c**, the foliation dip is shallow; however, it could also be horizontal or dipping into the slope **e** Foliation dip is shallow and a fault is present, rupture at the head of the slope utilises the fault plane (**f**)
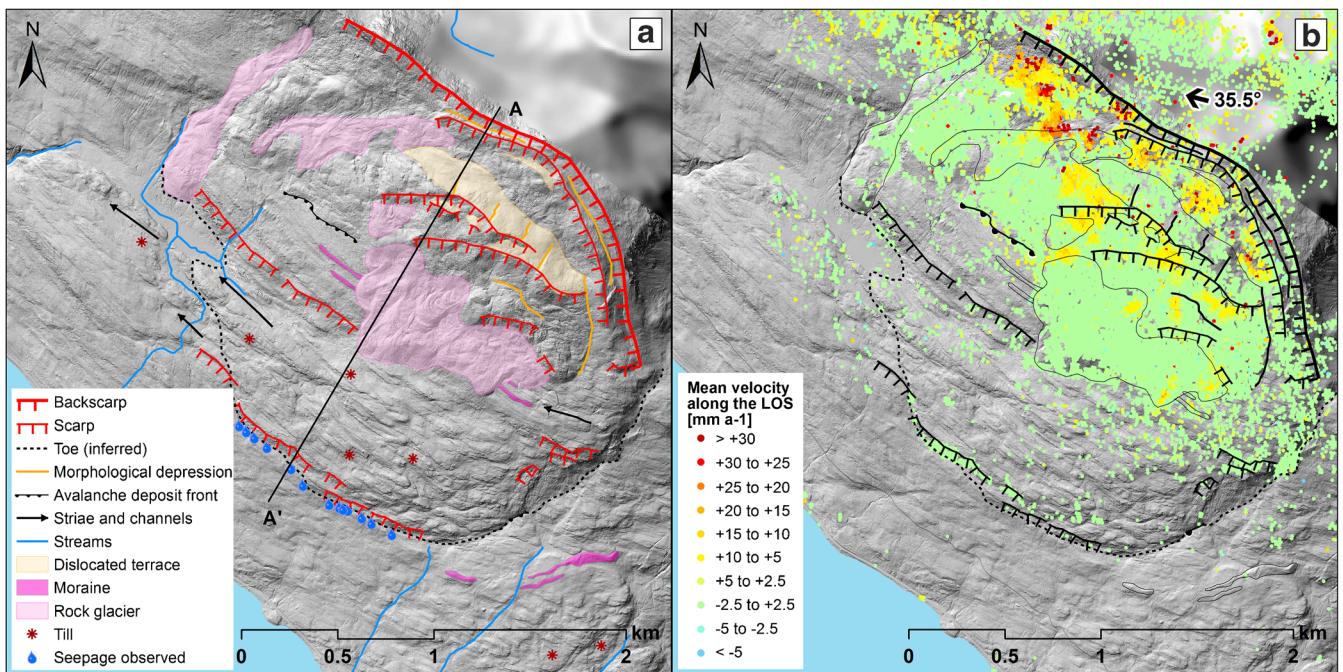
Fig. 4 **a** Morphostructure and location of A–A′ profile. **b** InSAR mean velocity [mm a^{-1}] along line-of-sight (LOS) in descending geometry (orientation of black arrow: LOS azimuth angle, label: LOS incidence angle; NGU 2019b). Background: hillshade based on 0.5 m ALS-derived digital elevation model
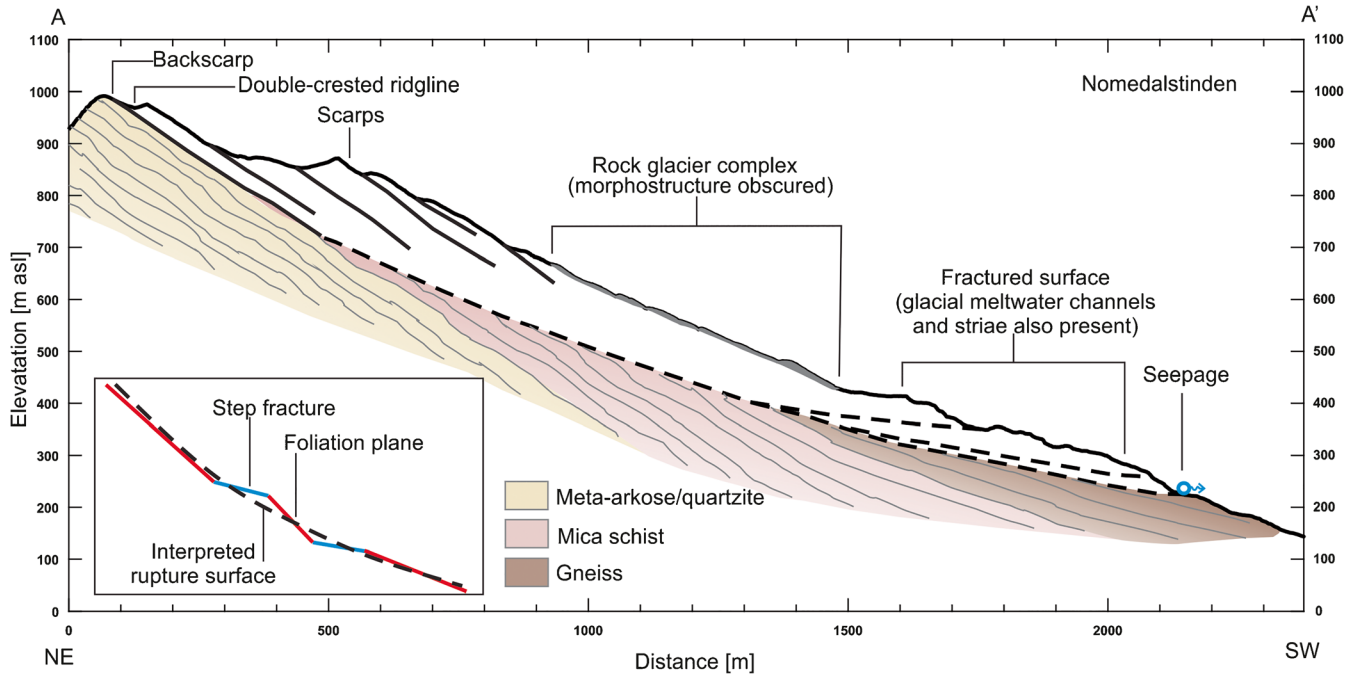
Fig. 5 A–A′ cross section of Nomedalstinden based on 0.5 m DEM (location on Fig. 4), showing exposed foliation-parallel sliding surfaces. Mapped rupture surfaces indicated by heavy black lines, and inferred rupture surfaces indicated by a dashed line. Inset is showing structural configuration of the rupture plane. Glacial geomorphology is based on Tolgensbakk and Sollid (1988) and geology on Zwaan et al. (2006)

however, there is a large talus supply in this area and it is difficult to separate signals from surficial and deep movement. The fastest moving objects are the upper parts of the western and eastern rock glaciers, moving up to > 30 mm a^{-1}.

Badjánanvárri
Badjánanvárri (Figs. 10 and 11) is adjacent to Rismmalčohkka and separated from it by the Litledalen cirque valley effectively segmenting the two peaks. The mountain comprises meta-arkose/quartzite, mica schists and banded gneiss (Zwaan et al. 2006). It slopes from 1169 m asl gently down to fjord level at an average of 20° from a plateau. The foliation dips 42° to the SW (Fig. 11), although it varies significantly locally. The backscarp dominantly follows foliation surfaces, but deviates in sections where local foliation structure varies. The backscarp is up to 50 m high and 1 km long. Badjánanvárri displays a series of down-shifted terraces with wide (< 450 m), intact surfaces (Figs. 10, 11 and 12) which are less disintegrated in appearance than the neighbouring Rismmalčohkka. The terraces are segmented by approximately foliation-parallel scarps, which in some cases can be traced down into the slope profile in the western valley where it offsets surficial deposits (Fig. 12). The main terrace displays some lateral spread towards the east (Fig. 12a). The lowermost terrace is delineated by steep high scarps formed by multiple avalanche events. Avalanche deposits extend from the front of the scarp to the lower reaches of the slope. Some of these deposits are mapped as active rock glaciers (Tolgensbakk and Sollid 1988). Some glacial geomorphic features are also identified in the central and lower slope.

On the eastern side of the slope, a pronounced ledge marks the lithological transition from mica schist to gneiss, with the ledge being comprised of gneiss (Fig. 12). Below this ledge is difficult to identify any clear signs of deformation in the intact bedrock.

While a toe line has been inferred (Figs. 10 and 11), surficial deposits make it difficult to delineate any evidence of compression. It is possible that the rupture path is less developed within the lower gneisses than the above schistose material. The slope surface is significantly shallower than the foliation dip, and therefore, the rupture surface would require a combination of foliation (as mapped at the scarp) and low-angled step fractures to achieve daylighting in the surface, regardless of where in the profile it may daylight.

The InSAR data (Fig. 10b) shows some errors on the terrace surfaces. By filtering these out, an average displacement of ∼ 4 mm a^{-1} at the lower terrace and ∼ 3 mm a^{-1} at the upper terrace is measured. Stable ground behind the backscarp also shows ∼ 2 mm a^{-1} displacement. The highest velocities (> 30 mm a^{-1} along LOS) are recorded at the rock glaciers and in some other areas of surficial activity, highlighting the active processes.

Joint-controlled rear rupture
At slopes where foliation angle is too shallow for rupture initiation or where it dips into the slope, the rupture must find another path. Steep discontinuities allow a tensile or shear release of metastable rock mass from the slope and can be existing joints or newly formed fractures. The weight of the unstable mass under tension will apply a force that allows for sliding on low-angled planes such as shallow foliation or step fractures generated during deformation (Glastonbury and Fell 2010; Stead and Eberhardt 2013). Joints
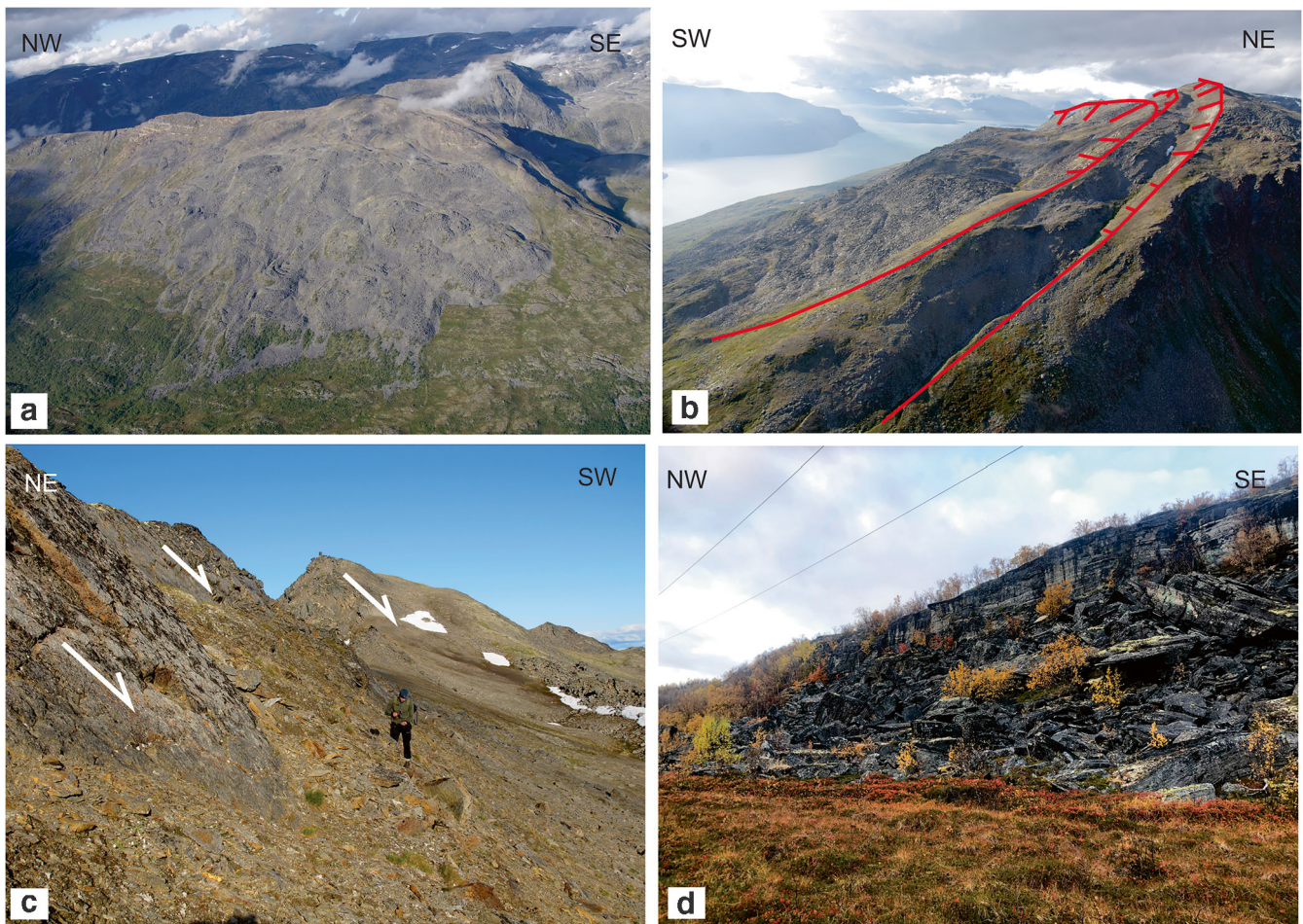
Fig. 6 **a** Overview photo of Nomedalstinden (Hermanns 2016). **b** View across double-crested ridgeline (Hermanns 2016). **c** Headscarp structure as exposed foliation plane (Bergh 2010). **d** Cliff face representing inferred toe of the slide. Small streams were observed seeping from the base of the cliff (Vick 2019)

in the mapping area generally strike NNE–SSW, ENE–WSW and NW–SE at near-vertical dip, an effect of fault formation during the rifting of the Norwegian margin (Bergh et al. 2007). Backscarps are accommodating a zig-zag rupture surface trace on W-facing slopes and a strike-parallel rupture surface on SW-facing slopes. The three sites categorised as joint-controlled rear rupture in this review all exhibit low-angled foliation dipping out of the slope.

Gámanjunni-3

Gámanjunni-3 is the third in a ridgeline series of four unstable slopes on the SW-facing flank of the Manndalen valley (NGU 2019a). The site has a >1/100-year probability of catastrophic failure and is considered a very high-risk object due to its characteristics and its location above dwellings, an access road and the Manndalselva River. The site has been the subject of ongoing investigations and continuous monitoring in recent years (Henderson et al. 2011; Bunkholt et al. 2012, 2013b; Hermanns et al. 2012; Böhme et al. 2016a, b, 2019; Eriksen 2017; Eriksen et al. 2017b). The failure scenario that is considered most likely and which has been accounted for the hazard assessment is estimated to be 26 Mm³ in volume (NGU 2019a).

Gámanjunni-3 stretches from the edge of the Gámanjunni plateau at 1217 m asl, to ca 570 m asl at an average slope angle of 35° to the WSW. The unstable area consists of Kåfjord Nappe mica schists with varying amounts of biotite and muscovite and calcareous schist of the Váddás Nappe below (Quenardel and Zwaan 2008). Foliation dips gently (average 8°) to NW, obliquely downslope. It is delimited by a striking 'V'-shaped backscarp formed by two scarps trending NW–SE and NE–SW forming a wedge with an intersection line of 45° plunge towards the valley (Böhme et al. 2016b, 2019) and clear lateral limits (Fig. 13). The unstable area is moving downslope as a coherent mass with an intact terrace at the top. The mass is moving along the wedge intersection, exposing the backscarps by the downshift of the top block by 150 m (Fig. 14).

A series of minor scarps form a step surface pattern down the length of the northern half of the RSD. The scarps give way to talus from rock fall and avalanches towards the southern half of the RSD. A rock glacier is mapped as active within these deposits (Böhme et al. 2019). The lower limit (western side) of the RSD is heavily fractured and fringed with a talus apron from ongoing rockfall activity. Uniquely, this RSD has a very clear toe, with thrusting at the lower boundary clearly indicated by a surface
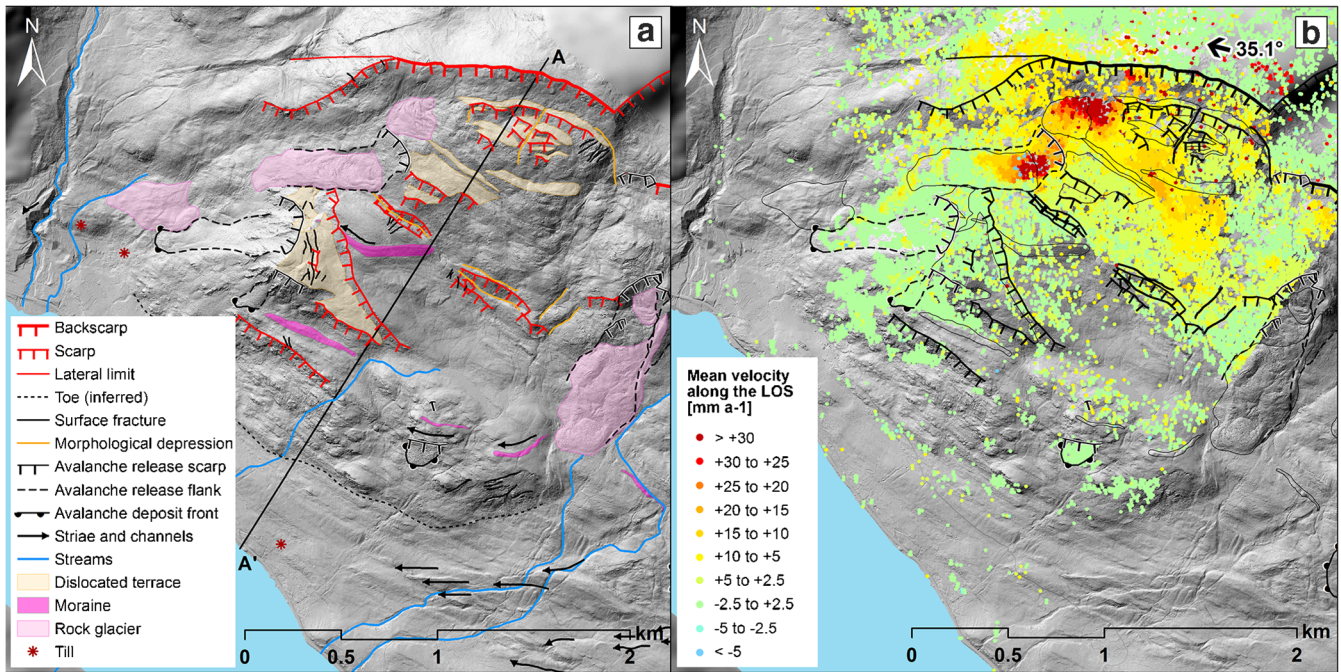
Fig. 7 **a** Morphostructure and location of A–A′ profile. **b** InSAR mean velocity [mm a^{-1}] along line-of-sight (LOS) in descending geometry (orientation of black arrow: LOS azimuth angle, label: LOS incidence angle; NGU 2019b). Background: hillshade based on 0.5 m ALS-derived digital elevation model

buckle and by upturned foliation. It is logical that the basal rupture surface traces around the base of this thrusted material. Discolouration of the rock material is seen in the lower half of the exposed toe (Fig. 15c), indicating channelisation of groundwater along the basal rupture.

Exposure dating of the backscarp shows that movement of the rockslide initiated during a warmer period of the Holocene, ca

5.3 ka, and has been moving at an average rate of 28 mm a^{-1} until recently (current maximum displacement is 54 mm a^{-1}; Böhme et al. 2019). It is currently one of the five fastest moving RSDs in Norway (NVE 2019).

The InSAR LOS is subparallel to the slope, good for movement detection (black arrow, Fig. 13b). However, parts are decorrelated due to fast and nonlinear displacement rates (e.g. the rock glacier in the
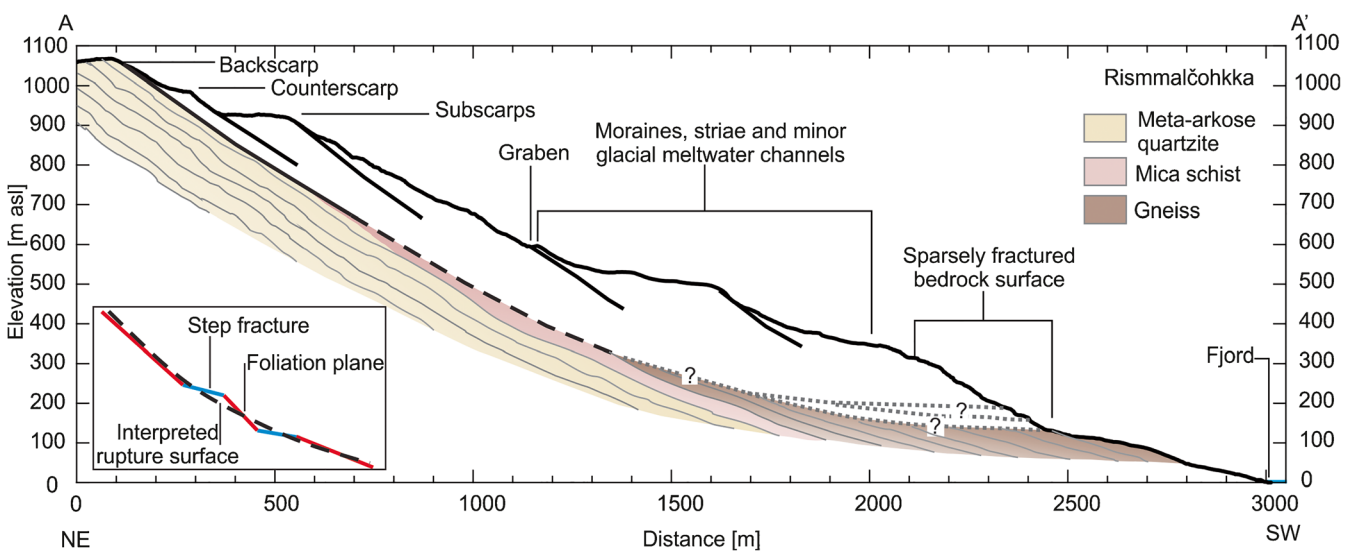
Fig. 8 A–A′ cross section of Rismmalčohkka, based on 0.5 m DEM (location on Fig. 7), showing exposed foliation-parallel sliding surfaces. Mapped rupture surfaces indicated by heavy black lines, inferred rupture planes indicated by a dashed line, uncertain rupture surfaces by a dotted line. Inset is showing structural configuration of the rupture plane. Glacial geomorphology is based on Tolgensbakk and Sollid (1988) and geology on Zwaan et al. (2006)
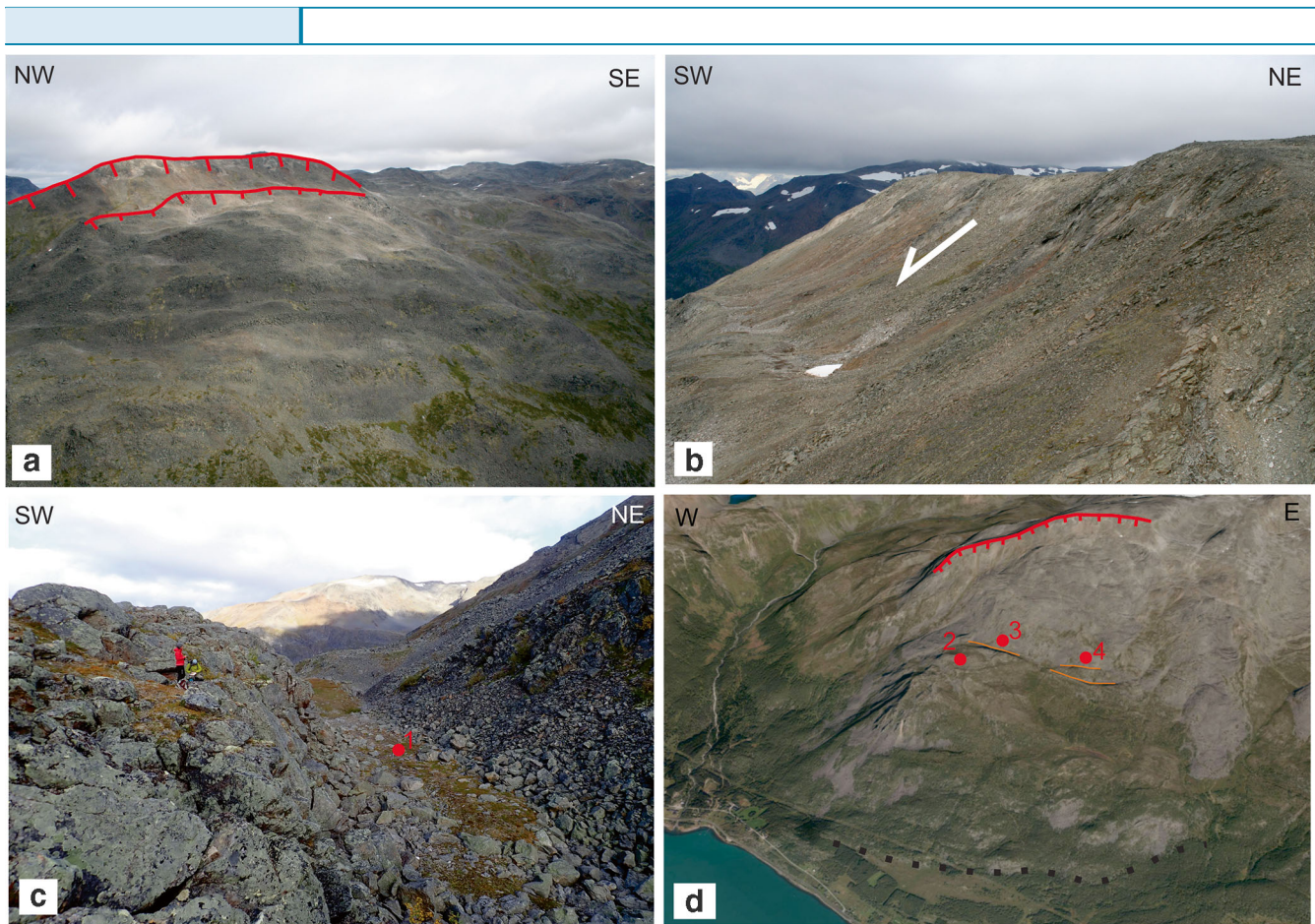
Fig. 9 **a** Overview photo of Rismmalčohkka indicating the backscarp (Henderson 2007). **b** Looking across the exposed backscarp of Rismmalčohkka, indicating sliding direction and a thin dislocated terrace below (Henderson 2007). **c** A graben structure from the central slope, with the preserved surface of the graben indicated by 1 (Bredal 2018). **d** 3D overview of Rismmalčohkka. 2. Top of the bedrock knob, delimited by graben structures indicated by 3 and 4. Inferred toe indicated by dotted a black line (Kartverket 2019b)

south-eastern part). In general, InSAR here shows the rockslide to be moving quite fast, showing > 30 mm a^{-1} along LOS in the northern parts (Fig. 13b), which correlated well with GNSS showing an average of 45 mm a^{-1} in the upper part (Böhme et al. 2019). The moving area is well delineated by the limits of the unstable mass. Movement rates obtained in a previous study from TerraSAR-X InSAR data and ongoing dGNSS monitoring show velocity is highest at the top of the instability, up to 60 mm a^{-1} and down to 30 mm a^{-1} at the toe (Böhme et al. 2016b, 2019; Eriksen et al. 2017b). 2D InSAR- and GNSS-derived movement vectors show dip of displacement consistent with the plunge of the wedge intersection (ca 45°) in the main slide mass, and a shallowing of vector dip towards the slide front, consistent with outwards thrusting at the toe (Böhme et al. 2019; Eriksen et al. 2017b; Fig. 14). As the wedge intersection does not daylight in the slope, displacement must be transferred to a shallow-dipping plane, possibly foliation. This transformation between joints and a shallow foliation is not only confirmed by the lower movement rates at the toe, but also by the geomorphic toe buckle and 2D InSAR-derived vectors (Böhme et al. 2016b).

Váráš

Váráš (also named Humpen and Hompen) is located in the Signaldalen valley, above the Signaldalelva River and inland access road. Two possible scenarios are considered for failure:

failure of the entire unstable mass (scenario A), or failure of only the smaller block on the NW limit of the slide (scenario B; Fig. 18a). The volume estimate of A is 70 Mm³ and 1.3 Mm³ for B (NGU 2019a). Despite these volumes, the consequences connected to a potential failure are considered low (for A) to very low (B) due to the remoteness of the valley. The risk ranking for A is low and for B medium. The site has been investigated since 2008 (Henderson et al. 2010; Hannus 2012; Bunkholt et al. 2013a), and due to the proximity of the failure scenario to the river and dwellings, GNSS monitoring points were installed in 2010 (NGU 2019a).

The RSD sits below a cirque valley with surrounding peaks between 800 and 1500 m asl. The instability slopes from 620 m asl, at an average slope angle of 30° to the valley base. The area comprises of the Kåfjord and Vaddas Nappe, with a range of lithologies simplified to amphibolite and metagreywacke (Zwaan 1988). The Nappe thrust boundary daylights within the backscarp of the unstable area. Foliation is variable, but dominantly dips 20° to the SW, with localised horizontal sections (Hannus 2012). The RSD delineated by a prominent vertical ca 85-m-high and 1-km-long NW–SE-striking backscarp, and NNE–SSW-striking lateral (southern border) scarp. Both scarps align with locally dominant steeply dipping joint sets (Hannus 2012). Upslope several tension
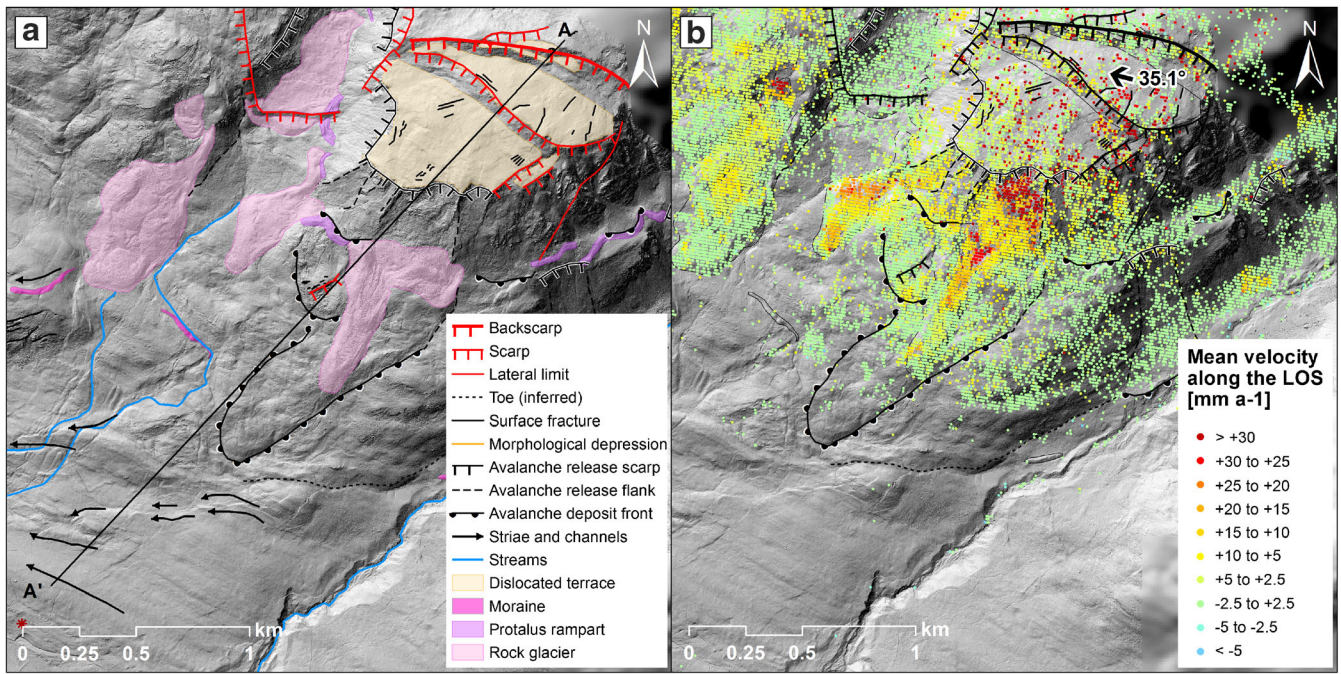
Fig. 10 **a** Morphostructure and location of A–A′ profile. **b** InSAR mean velocity [mm a⁻¹] along line-of-sight (LOS) in descending geometry (orientation of black arrow: LOS azimuth angle, label: LOS incidence angle; NGU 2019b). Background: hillshade based on 0.5 m ALS-derived digital elevation model

cracks also align with the main scarp and reach up to 500 m in length (Fig. 18b). The back scarp delimits a large graben (ca 85 m wide) that contains disaggregated rock and subsided blocks (Fig. 18c, d). Below this, multiple subsidiary scarps and counterscarps cut through the unstable area, aligning NW–SE with the main scarp (Fig. 18d). Although the instability is crosscut with scarps, in general, the main body appears to have sagged/relaxed as a cohesive mass.

Exposed bedrock in the lower slope is heavily fractured, and the fracture systems are difficult to map due to vegetation. The fractures are often open and appear as morphological depressions/ sinkholes where till cover is draped across. The slope toe follows the river channel in the north and an abandoned channel in the south, where glaciofluvial deposits have been mapped (NGU 2019a). Scenario B sits directly above where the present river channel cuts into the slope. A large rock avalanche deposit covers
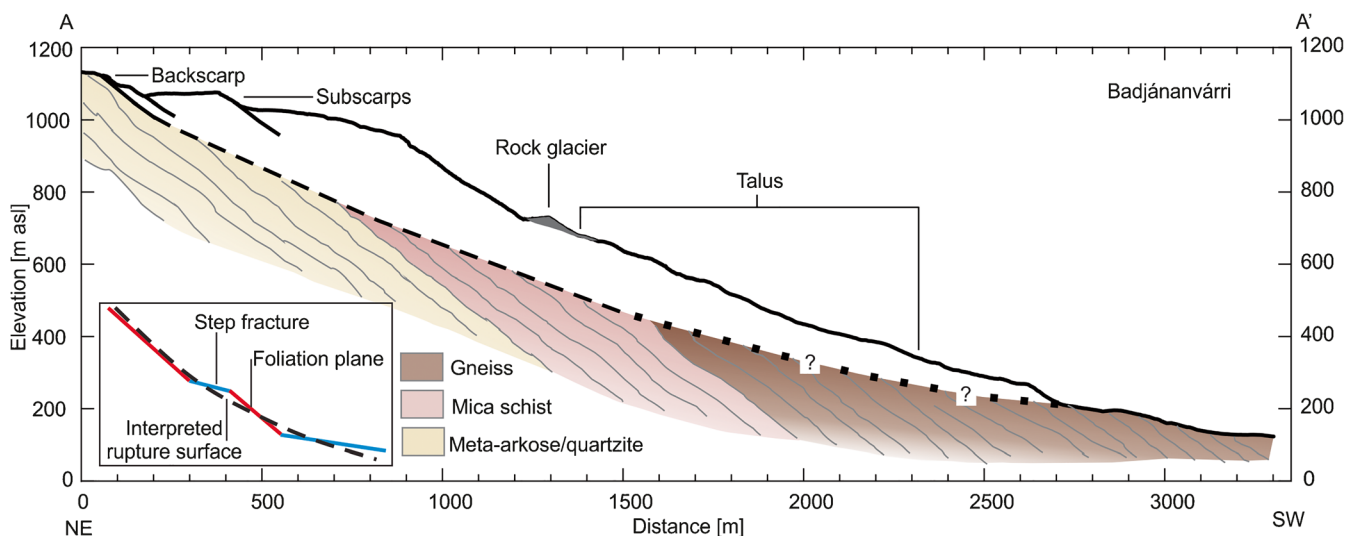
Fig. 11 A–A′ cross section of Badjananvarri, based on 0.5 m DEM (location on Fig. 10), showing exposed foliation-parallel sliding surfaces. Mapped rupture surfaces indicated by heavy black lines, inferred rupture planes indicated by a dashed line, uncertain rupture surfaces by a dotted line. Inset is showing structural configuration of the rupture plane. Glacial geomorphology is based on Tolgensbakk and Sollid (1988) and geology on Zwaan et al. (2006)
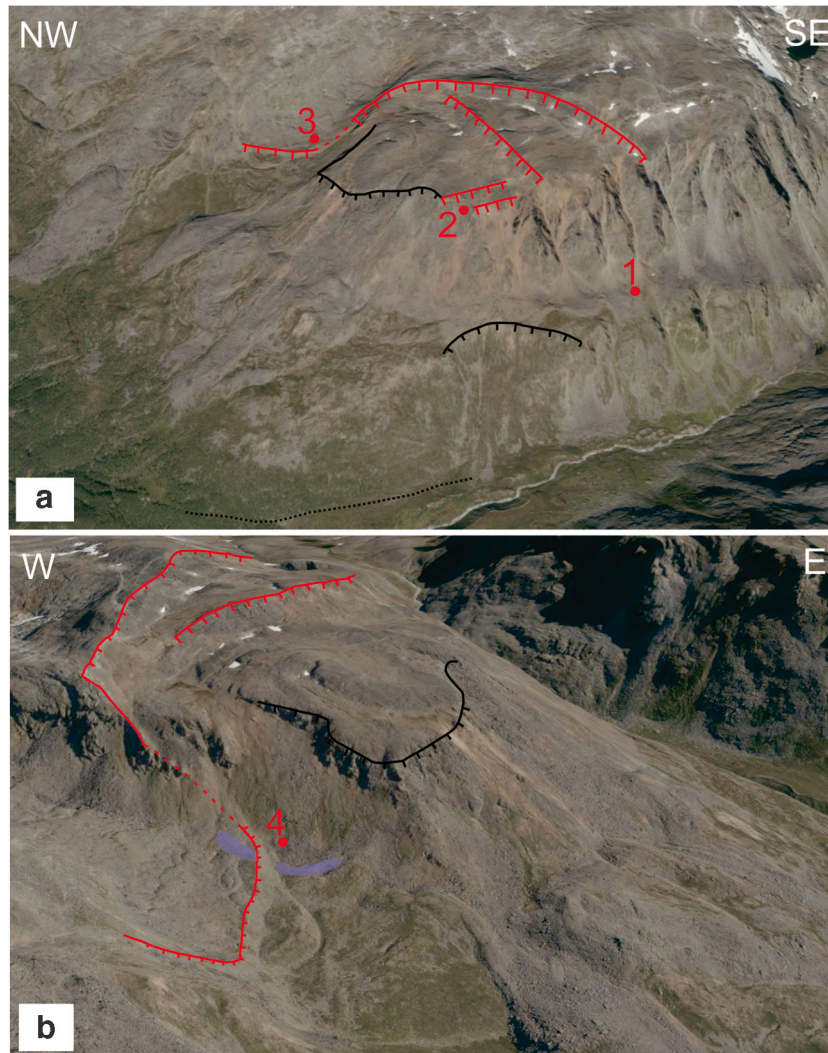
Fig. 12 a A view of Badjánanvárri to the NE, showing scarps (red) and avalanche release areas (black). 1 indicates a ledge formed by the competence difference between the mica schist above and gneiss below. 2 indicates lateral spread of the main terrace into the valley E. 3 indicates the scarp which crosscuts the Litledalen valley towards Rismmalčohkka. The scarp offsets a rock glacier. **b** A view of Badjánanvárri to the N. 4 indicates a scarp offset of surficial deposits. Images captured from www.norgeibilder.no

most of the northern portion of unstable area below scenario B, indicating that oversteepening of the slope here has led to failure in this domain.

There is a clear buckle in the slope morphology of the mountain, delimited by an inferred toe line at the break before the valley floor (Fig. 16a). Groundwater seeping from the bedrock around the toe has been observed in early summer (Hannus 2012). The inferred toe indicates a possible daylighting basal rupture surface; however, it could also be buried under fluvial sediments deeper within the valley. To daylight in either case, the rupture surface must transfer from steep surfaces at the rear, to low-angle surfaces at the base. The foliation is locally poorly developed, as well as irregular, folded and containing lenses and boudins (Hannus 2012). In some locations, foliation is mapped as horizontal or even dipping into the slope. It is therefore likely that the basal rupture surface comprises step fractures, as well as foliation and joint surfaces (Fig. 17 insert). Forward rotation of the unstable mass

has led to the formation of the graben structure, as well as the series of counterscarps due to the driving force of the upper material on lower.

Flooding of the pond within the cirque valley (Fig. 18b) has led to episodes of debris flow and slush avalanches parallel to and outside of the lateral scarp (Hannus 2012). The tension cracks between the pond and the backscarp accommodate overflow drainage from the pond. Water fills the cracks until late summer, when the water rapidly draws down and both the cracks and the pond empty. Water can be heard flowing through the unstable area after drawdown of the cracks and pond, hinting at a fracture network linking the tension cracks and the unstable area accommodating groundwater flow. Ponded water and springs mapped at the toe in late spring are completely dry by late summer (Hannus 2012). It is likely there is some hydromechanical and seasonal control on the movement of the rockslide. Groundwater recharge is clearly seasonally controlled, and at times, the fracture network
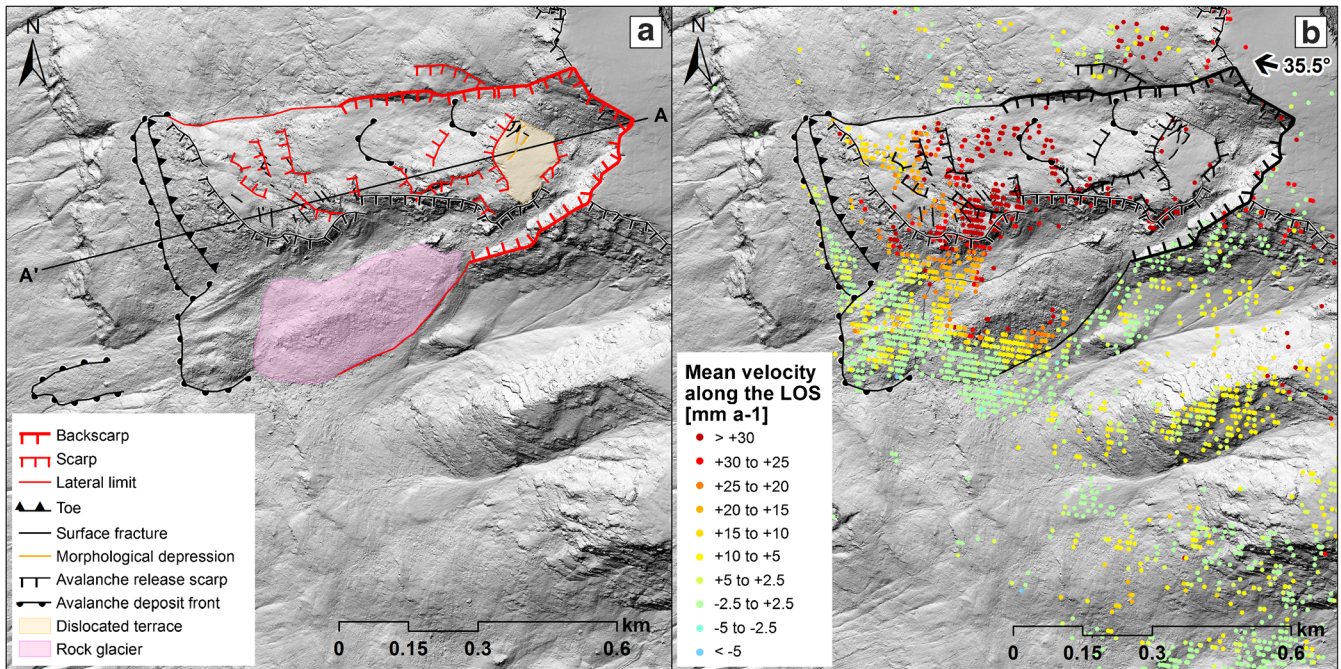
Fig. 13 a Morphostructure and location of A–A' profile. **b** InSAR mean velocity [mm a^{-1}] along line-of-sight (LOS) in descending geometry (orientation of black arrow: LOS azimuth angle, label: LOS incidence angle; NGU 2019b). Background: hillshade based on 0.5 m ALS-derived digital elevation model

in the unstable area is flooded or flushed which may lead to short bursts of deformation.

dGNSS measurements within the unstable area show horizontal movements between 2 and 3 mm a^{-1} towards the SW of scenario A. For scenario B, the GPS measurements show a speed of 4 mm a^{-1}, also to the SW. Ground surface velocities from InSAR in the upper part of the main unstable area are between 2.5 and 5 mm a^{-1} along LOS, in line with dGNSS measurements, confirming that scenario A is not very active (Fig. 16). The highest movements are detected at and below scenario B. Areas with velocities > 30 mm a^{-1} along LOS indicate superficial displacements in the avalanche deposit, while values between 5 and 15 mm a^{-1} at the scarp may correspond to the movement of the whole mass. Some movement (~ 2 mm a^{-1}) above the unstable area indicates that the instability could be retrogressing (after Cruden and Varnes 1996) and that tension cracks are symptomatic of this. However, this small value could be due to data error and dGNSS above the unstable area shows negligible vertical and horizontal movement.

Oksfjellet

Oksfjellet is located on the SW flank of Kåfjord, opposite to Nomedalstinden, Rismmalčohkka and Badjánanvárri. The SW flank of the valley differs from the gentle ca 20° slopes in the NW flank—the slopes are steep to near-vertical exposed cliff sections. The RSD lies above dwellings, the Kåfjord River and adjacent to the town of Birtavarri. The failure scenario is estimated to be 5.3 Mm³ in volume and ranked medium risk (NGU 2019a).

The area slopes from a plateau at 1115 m, through the unstable area at an angle of 35°, through a cliff section at an angle of ca 70°, and down through a talus slope to the valley floor which dips on average 30°. A major thrust nappe boundary runs through the

Oksfjellet cliff exposure, separating the Vaddas and Kåfjord Nappe. The rock on either side of the boundary comprises mica schists with varying contents of biotite, muscovite, garnet, quartzite and feldspar (Quenardel and Zwaan 2008). Oksfjellet differs from other sites reviewed here, as it does not display cataclinal foliation. The foliation dips NW, perpendicular to the slope. It varies locally between 15 and 40. Discontinuities within the RSD general area align with NNE–SSW to NE–SW and NW–SE trending regional brittle structures.

The backscarp bounding the main unstable area aligns overall NW–SE, parallel to the valley (Fig. 19). It is comprised of steeply dipping orthogonal discontinuities (70–85°) dipping to the NW and NE in a zig-zag fashion (Bredal 2016). The scarp is 50 m high in the centre and decreases in height towards the lateral margins. The main displacing block at Oksfjellet is indicated by the terrace surface in Fig. 19. The unstable material is offset from the backscarp by an up to 100 m wide graben structure containing talus as well as a series of smaller scarps and counterscarps (Figs. 20 and 21d). The scarps and counterscarps strike joint-parallel, and smaller graben structures are observed between these. To the SW of the backscarp, open fractures and minor scarps crosscutting the plateau strike NW–SE and NNE–SSW. Some cracks and poorly developed scarps are also found to the NW of the main displacing block.

The thrust boundary runs through the lower part of the unstable area. It follows a monocline structure ramping up to 40° at the SE boundary (Fig. 21a). A wedge slide is formed by this thrust and the NW lateral limit, while the back scarp forms the rear release structure. The toe line is defined based on GB-InSAR, which indicates deformation down to the underlying thrust plane, but not below.
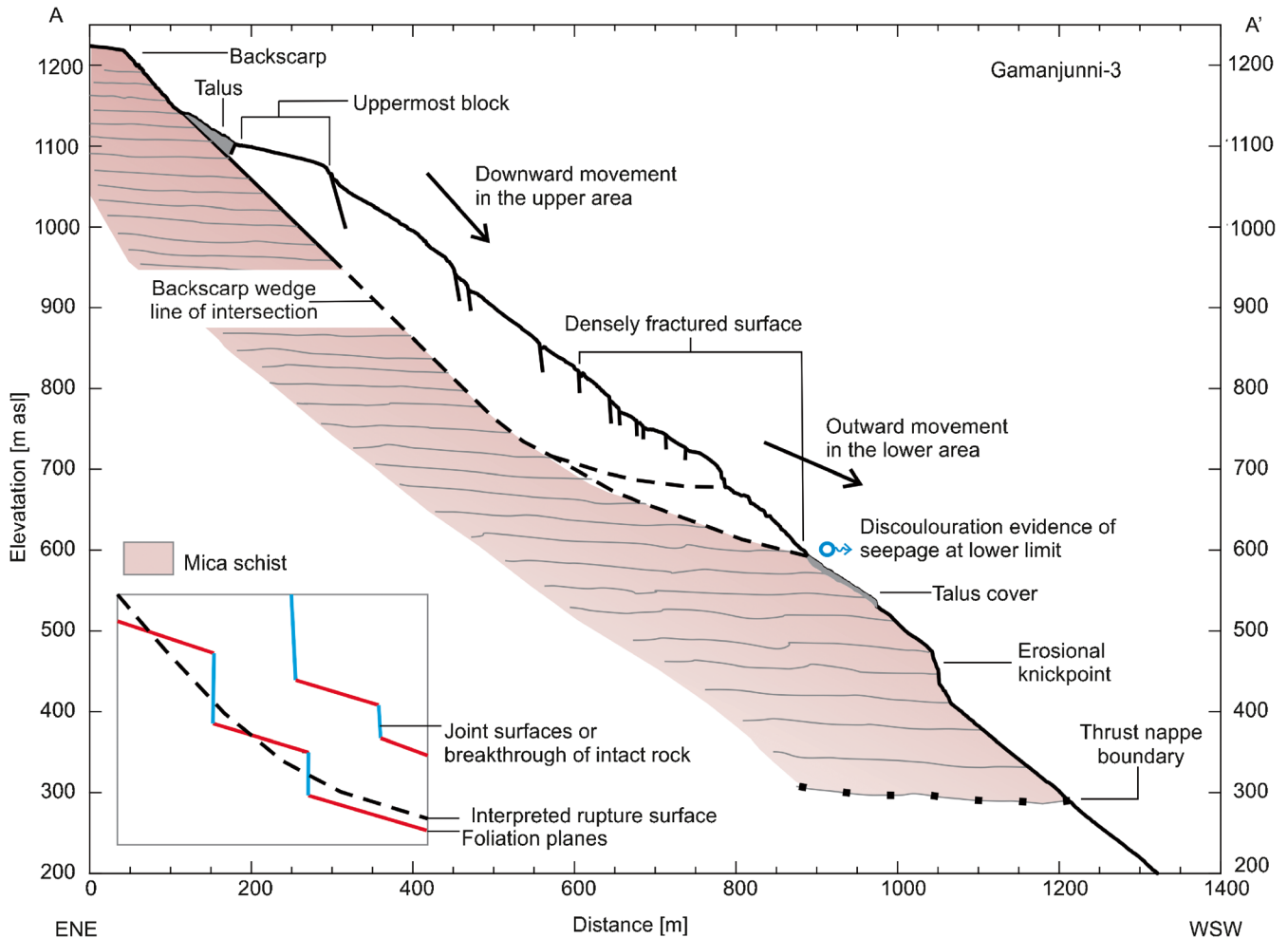
Fig. 14 A–A' cross section of Gámanjunni-3, based on 0.5 m DEM (location on Fig. 13), showing exposed rupture planes. Mapped rupture planes indicated by heavy black lines, and inferred rupture planes indicated by a dashed line. Movement vectors (black arrow) derived from 2D InSAR (Eriksen et al. 2017b). Geology based on Quenardel and Zwaan (2008)

InSAR results highlight a coherent pattern within the main unstable area, with low velocities between 2.5 and 5 mm a^{-1} along LOS (Fig. 19b). This is in line with dGNSS measurements (3–4 mm a^{-1}). The clear relationship between movement and geological structures is also evidenced by a study combining satellite and ground-based InSAR (Bredal, 2016). GB-InSAR campaigns detected higher rates (up to several mm day^{-1}) at isolated locations in the deposit area below the main unstable area. The overall movement of the RSD showed significant displacement to horizontally to the NE in earlier campaigns; however, the vertical trend became clearer in more recent years and indicates a downward dip of 10–20° (NGU 2019a).

Fault-controlled rear rupture

A series of faults striking NE–SW and dipping steeply NW crosscut the region. In three cases where these structures occur in W- and NW-facing slopes, a rockslide has developed (Fig. 1). In all three cases, foliation dips shallowly out of the slope.

Jettan

Jettan is an RSD within the Nordnesfjellet ridgeline—a fjord flank which slopes from a plateau at 861 m asl at an average of 35°. The RSD lies between 700 m asl and fjord level. Jettan is the fastest moving in a series of RSD along the same flank. The rockslide is estimated to be up to 17 Mm^3 (6 Mm^3 in the most realistic scenario). The annual probability of a catastrophic failure is estimated at between 1/100 and 1/1000, with major consequences from a displacement wave to villages lining the shores of Storfjord (Glimsdal and Løvholt 2018; NVE 2019). For this reason, Jettan is considered a 'high-risk object' (NVE 2019). The site has been continuously monitored from 2007, with installations of GNSS, laser, extensometers, ground-based radar (GB-InSAR), satellite corner reflectors, borehole instrumentation measuring displacement, water levels, temperature and vibrations (differential monitoring of stability, DMS), tiltmeters, meteorological station and web cameras (NVE 2019). The slide has been the subject of studies, investigations and theses since 1999 (Braathen et al. 2004; Blikra et al. 2006a, b, 2009; Rønning et al. 2008; Blikra and Longva 2009; Nordvik et al. 2010; Ganerød 2013a, b; Skrede 2013; Elvebakk 2013, 2014; Blikra and Christiansen 2014; Eriksen et al. 2017a, b; Eckerstorfer et al. 2018).

The slope comprises mica schists interbedded with a layered metasedimentary sequence of calcite marble and meta sandstone
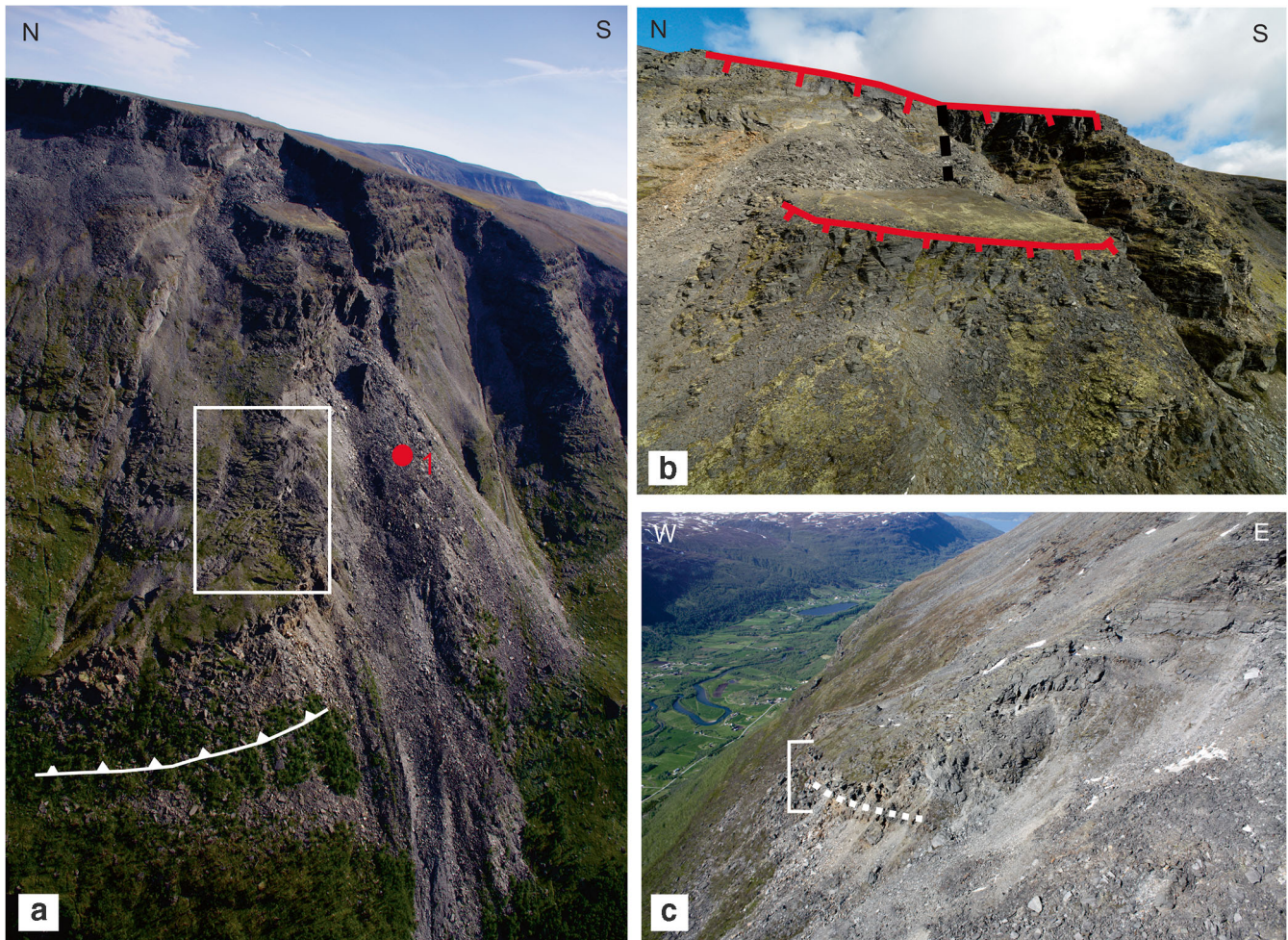
Fig. 15 **a** Overview photo of Gámanjunni-3 from the south (Bunkholt 2010). White box indicates area of high surface fracture density, toe indicated by a white line. 1 indicates rock glacier. **b** Backscarps and uppermost block surface (Solberg 2013). Black line indicates daylighted wedge intersection of orthogonal backscarps. **c** Toe buckle/ thrust of the rockslide indicated by bracket (Bunkholt et al. 2012). White dash indicates line below which rock material is heavily oxidised indicating channelisation of groundwater flow along the basal rupture

of the Nordmannvik Nappe. The Nappe boundary daylights in the slope at ca 275 m asl, with garnet schist of the Kåfjord Nappe below (Zwaan et al. 2006). Foliation dips gently towards the fjord (NW) ≤17° (Braathen et al. 2004; Skrede 2013; Eriksen et al. 2017a). The unstable mass is delineated by prominent steep orthogonal backscarps dipping NW and SW forming a 'V' shape (Fig. 22). The NW-dipping scarp is interpreted as an inherited normal fault dipping 60–70° (e.g. Blikra and Christiansen 2014; Braathen et al. 2004; Skrede 2013), as it offsets the lithostratigraphy (Zwaan et al. 2006). The SW-dipping scarp is comprised of steeply dipping near-vertical joint sets striking dominantly NW–SE. The intersection of the two backscarps plunges steeply (64°) in a WNW trend (297°). Scarps throughout the RSD repeat the same V-shaped structural pattern as the backscarps, striking NW–SE and NE–SW (Fig. 23).

Some deformation is taking place above the backscarps (Fig. 22). The surface fractures are large open crevasses within a marble cap that sits on top of the RSD. Subsidence of the unstable mass (which

has split the cap in two) has allowed the upper half/in situ part of the cap to relax, causing and opening of joints within the material. The lower half of the marble cap, within the unstable mass, is identified as a rock glacier (Blikra and Christiansen 2014). The N domain of the RSD is a chaotic 'block field' of many small dislocated and rotated terraces, as well as disintegrated blocky material indicative of past collapse events (Fig. 24c). In the central area, a terrace assemblage forms a stepped surface (Fig. 24b). Within these terrace surfaces, till is draped over large open fractures in the bedrock, creating lines of sinkholes mapped as morphological depressions. Deep open fractures which are not obscured by deposits are observed to be controlled by joint orientation, and often contain ice year-round. The lower half of the RSD is covered with thick talus (rockfall debris and small avalanche deposits) and gives way to a large toe buckle near fjord level (Fig. 22). Previous events at the neighbouring rockslide Midtre Nordnes have been noted from marine geophysical and coring investigations in the fjord below, with an avalanche deposit
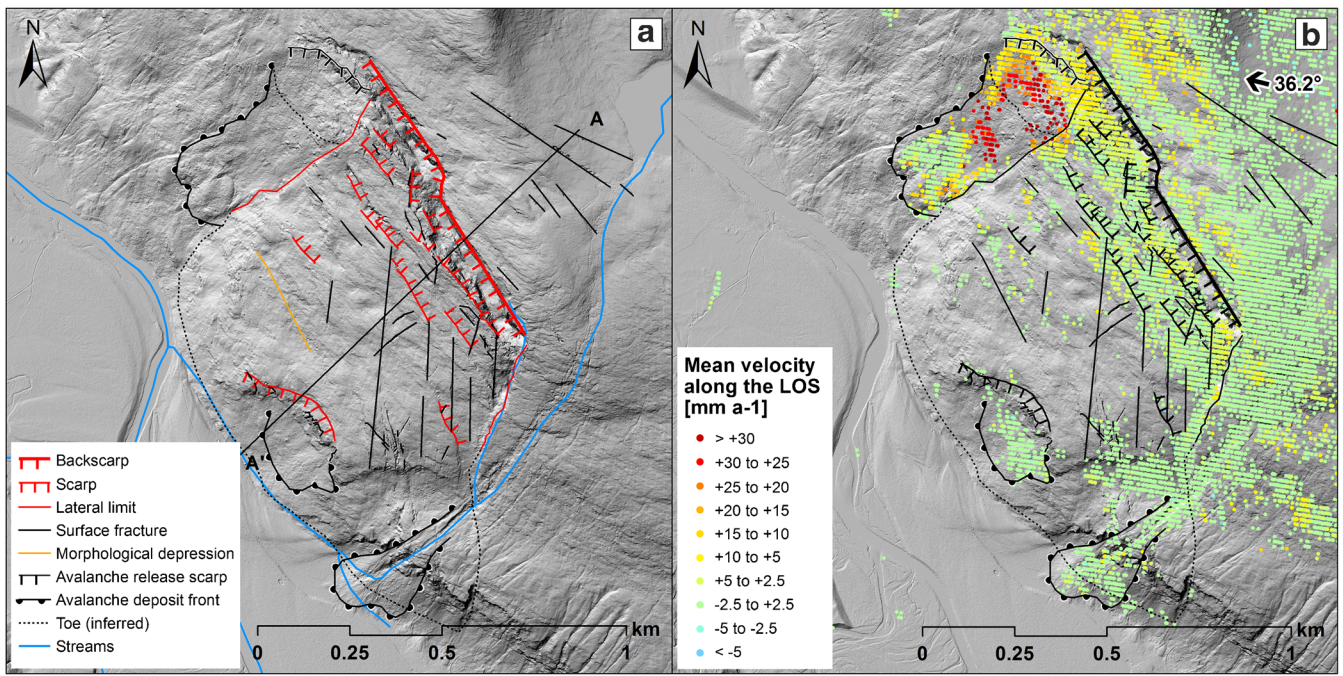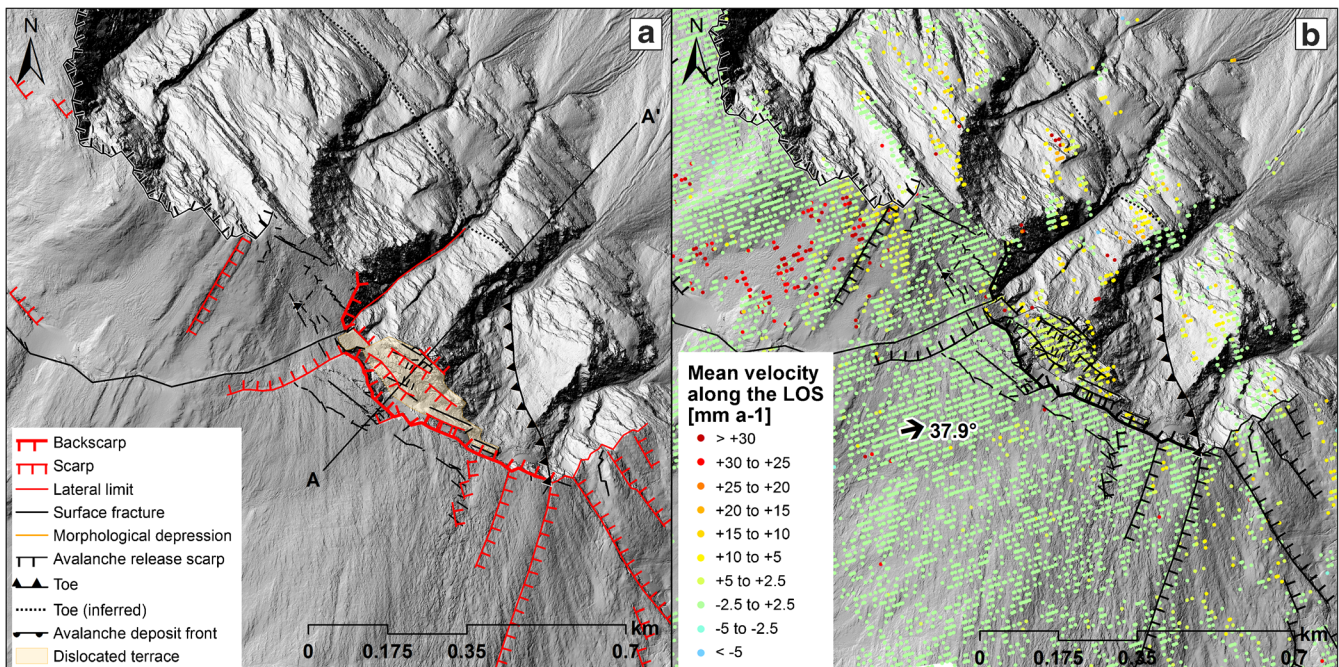
Fig. 16 **a** Morphostructure and location of A–A' profile. **b** InSAR mean velocity [mm a^{-1}] along line-of-sight (LOS) in descending geometry (orientation of black arrow: LOS azimuth angle, label: LOS incidence angle; NGU 2019b). Background: hillshade based on 0.5 m ALS-derived digital elevation model
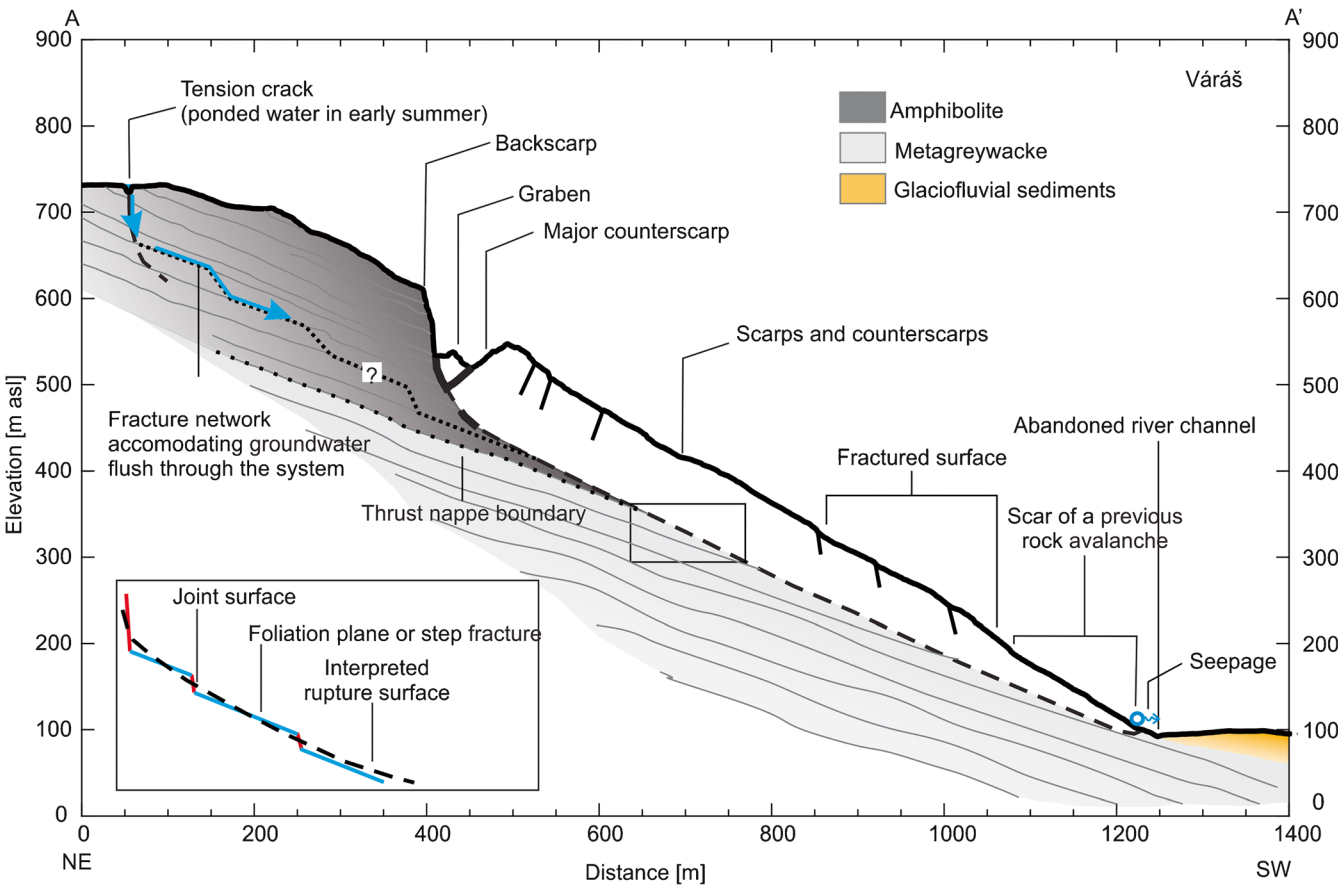
Fig. 17 A–A' cross section of Váráš, based on 0.5 m DEM, showing exposed joint-parallel backscarp (location on Fig. 16). Mapped rupture planes indicated by heavy black lines, and inferred rupture planes indicated by a dashed line. Inset is showing structural configuration of the rupture plane. Geology from Zwaan (1988)
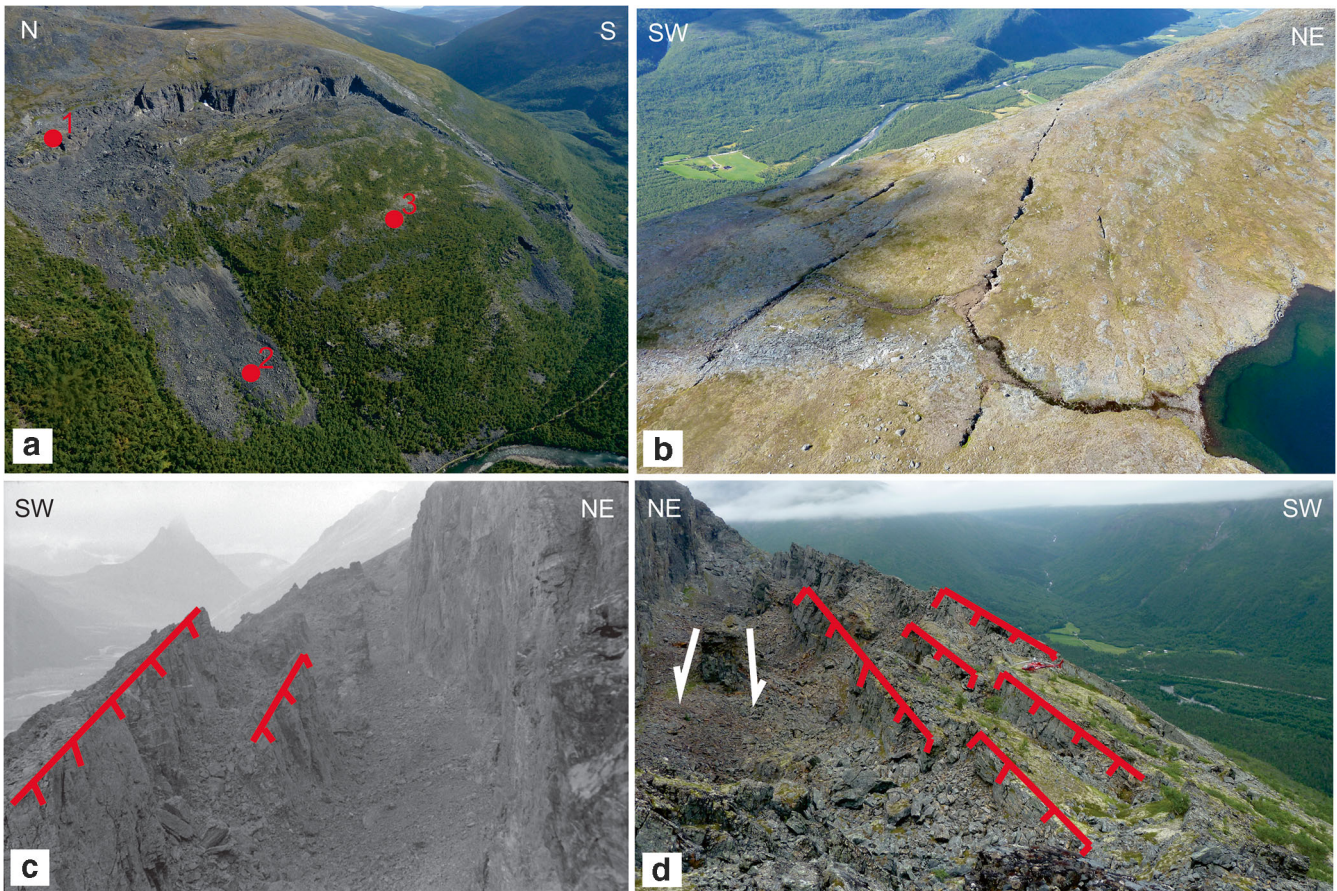
Fig. 18 **a** Overview photo of Váráš (Bunkholt 2011). Annotation indicates the smaller block of scenario B (1), and previous avalanche events below scenario B (2) and the main unstable area, scenario A (3). **b** Tension cracks upslope of the unstable area accommodate through-going drainage fed by the lake (Bunkholt 2011). **c** Backscarp and counterscarp (Corner 1969). **d** Backscarp, graben and counterscarps formed by downslope movement of unstable mass and subsidence of graben material (Bunkholt 2010)

Fig. 19 **a** Morphostructure and location of A–A' profile. **b** InSAR mean velocity [mm/year] along line-of-sight (LOS) in ascending geometry (orientation of black arrow: LOS azimuth angle, label: LOS incidence angle; NGU 2019b). Background: hillshade based on 0.5 m ALS-derived digital elevation model
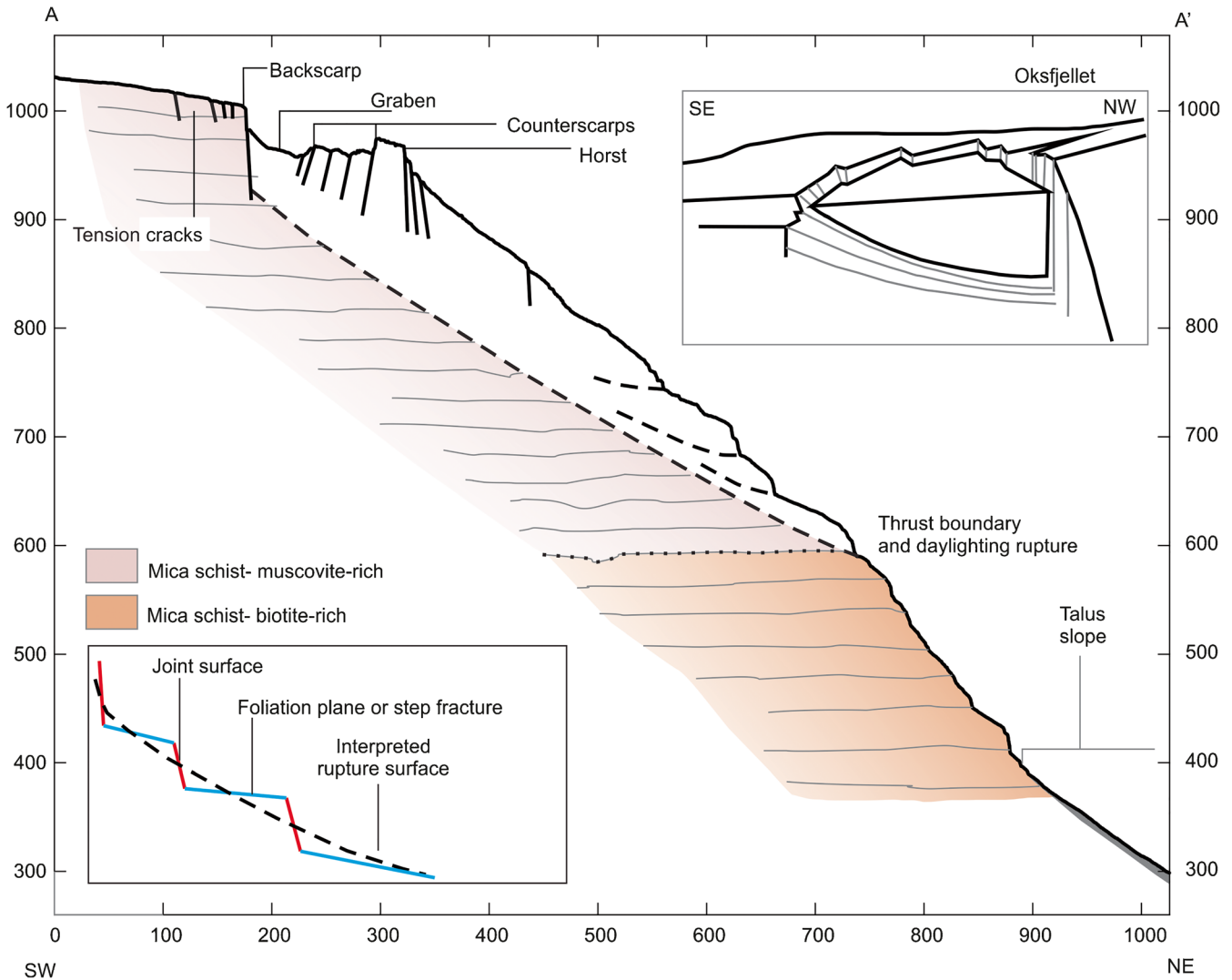
Fig. 20 A–A′ cross section of Oksfjellet, based on 0.5 m DEM (location on Fig. 19). Mapped rupture planes indicated by heavy black lines, and inferred rupture planes indicated by a dashed line. Inset is showing a simplified 3D model of the main sliding block and sliding planes, after Bredal (2016). Geology from Quenardel and Zwaan (2008)

complex showing that a period of mass wasting occurred around 10,800 cal. years BP (Hegstad 2014).

There are likely multiple basal rupture surfaces at depth. Borehole data (Ganerød 2013a, b) and downhole geophysics (Elvebakk 2013, 2014) show multiple crush zones at irregular depths containing brecciated rock and clay material. The 'main zone of deformation' occurs as repeated layers of breccia and clay seams in mica-rich rock between 42 and 46 m below ground level (bgl) in BH1 and between 36 and 53 m bgl in BH3 (Ganerød 2013a). Swelling clays were recorded in the crush zones from X-ray diffraction analysis (110–145% free swelling of clay; Nystad 2015). Surfaces bounding crush zones dip between 19 and 81° out of the slope, but most dominantly dip between 20 and 40°. This aligns with rock mechanical testing which demonstrated a basic friction angle in the material of between 31 and 34° (Nystad 2015). It is likely that multiple levels of rocksliding have developed within the major bounding rupture limit (Fig. 23).

The InSAR LOS is subparallel to the slope, good for movement detection (black arrow, Fig. 22b). Velocities from 15 up to > 30 mm a^{-1} along the LOS are detected. Other studies combining multiple SAR geometries highlighted a maximum of 50 mm a^{-1} downslope movement. Displacement vectors obtained from 3D InSAR and validated by dGNSS show surface movement mainly oriented to the WNW (Eriksen et al. 2017a). Additionally, vectors display a deep downward dip in the upper slope and a shallow outward dip in the lower slope (Fig. 23), indicating that rupture surfaces become listric with depth. The velocity of the slide reduces downslope, indicating compression and thrusting.

Movement of the rockslide has been linked to seasonal displacements, the largest occurring just after snowmelt and slowing again in early winter (Nordvik et al. 2010; Blikra and Christiansen 2014). Snowmelt in spring and early summer are known triggers for rockslide movement accelerations; however, in this case,
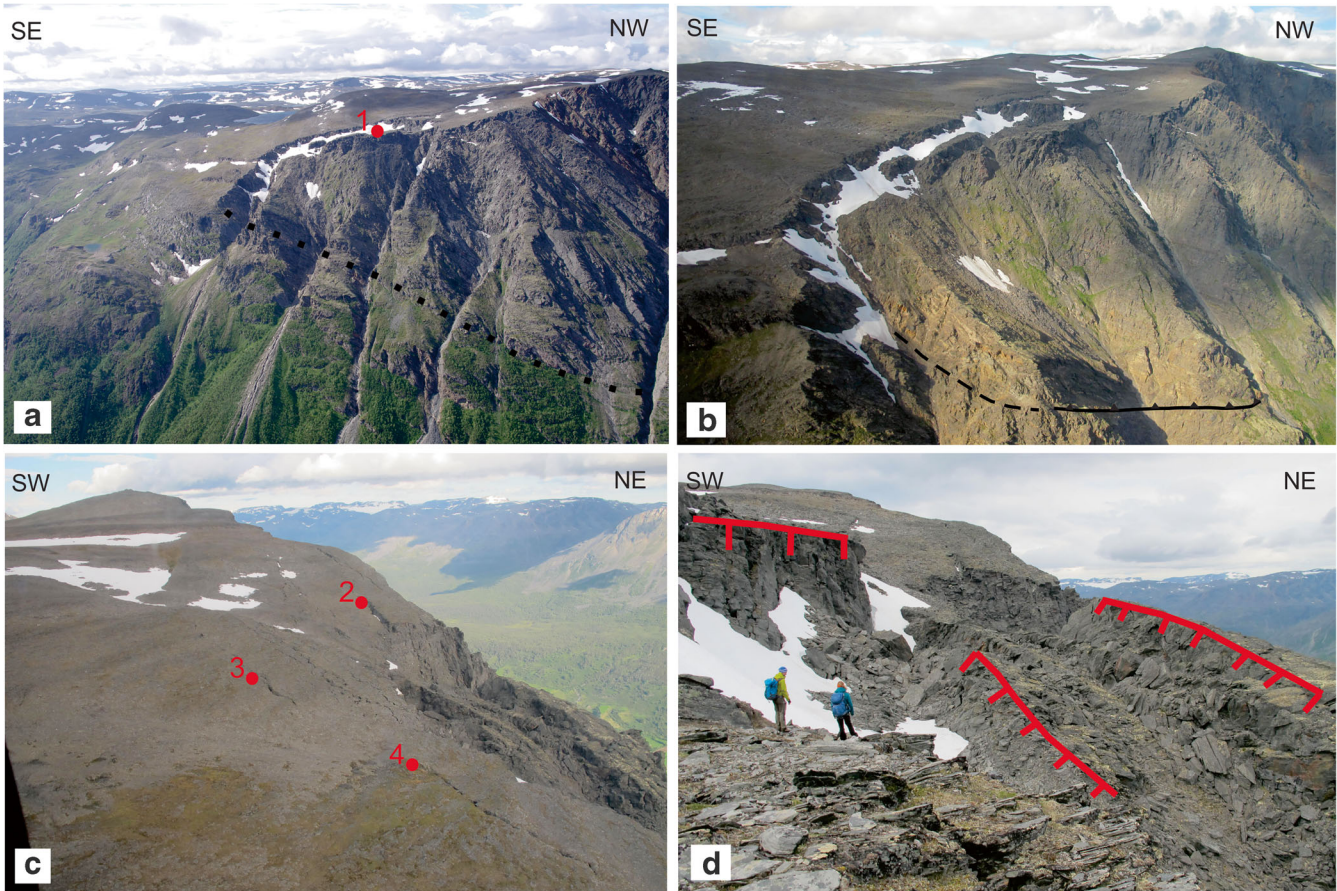
Fig. 21 **a** Overview photo of the Oksfjellet cliff section showing approximate thrust nappe boundary and terrace of main displaced block (1) (Böhme 2015). **b** Overview of the active Oksfjellet block showing the basal rupture surface (Bergh 2015). **c** Looking down at the RSD (bottom right) and across the tension cracks (2–4) in the plateau (Bergh 2015). **d** Looking north along the backscarp of Oksfjellet, through the graben and across counterscarps (Bergh 2015)

accelerations in autumn are unexpected. They have been linked to permafrost processes, as the site is immediately below the regional discontinuous permafrost limit and deep fractures allow for cold air permeation, driving deformation as a consequence of freezing mechanisms.

Laksvatnfjellet

Laksvatnfjellet is the westernmost site in this study, separated from the others by the Lyngen Peninsula. It is above the town of Laksvatn and the Laksvatnet Lake and adjacent to several other settlements that are located close to sea level along Balsfjord. The ridge of the mountain slopes down from 875 m asl to the valley at an average slope angle of 25°. The unstable area comprises mica schist (granite schist with a presence of chlorite; Zwaan et al. 1998), with localised lenses of metagabbro and amphibolite (Rasmussen 2011). The foliation is folded and crenulated and dips between 10 and 35° predominantly NW but varies across the RSD, dipping to the E and SE in places. Dominant joint sets strike NE–SW and ENE–WSW, steeply dipping in oscillatory directions (Rasmussen 2011). The area contains a NE–SW-striking splayed fault, which dips 65° to the NW. A ca 50-cm-wide zone of strongly fractured rock and gouge has been mapped at this fault (Fig. 27c). Gouge and

slickenside striations have been dated to the late Devonian to early Carboniferous (Davids et al. 2013). The fault borders the S limit of the unstable area (Fig. 25) and splays near the peak of the mountain (Fig. 26 insert). The upper splay, fault splay 1, traces behind the mountain ridge. The lower splay, fault splay 2, is the backscarp of the RSD and contains fibre lineations which indicate episodes of movement prior to rock sliding. The backscarp section of the fault is a 1.9-km-long ca 30–40 m high and dips between 60° NW and vertical (Rasmussen 2011).

The unstable area displays a complex surface geometry with disparate morphostructure across the slope (Figs. 25 and 26). In the upper central portion, a series of counterscarps are below and parallel to the backscarp (Fig. 27a). The counterscarps delimit 'slabs' of rock which are sliding on foliation surfaces dipping locally around 35° downslope. The foliation above the backscarp (in the stable area) has been mapped as on average 20°, and this steeper area could therefore be a result of localised folding. The slabs appear to be sliding on weaker layers of phyllite (Fig. 27e). These give way to dislocated and rafted terraces forming a stepped geometry (Fig. 27b). The terraces show break up and movement both directly downslope and laterally. They display open surface fracturing and sinkhole morphology from till draped over open
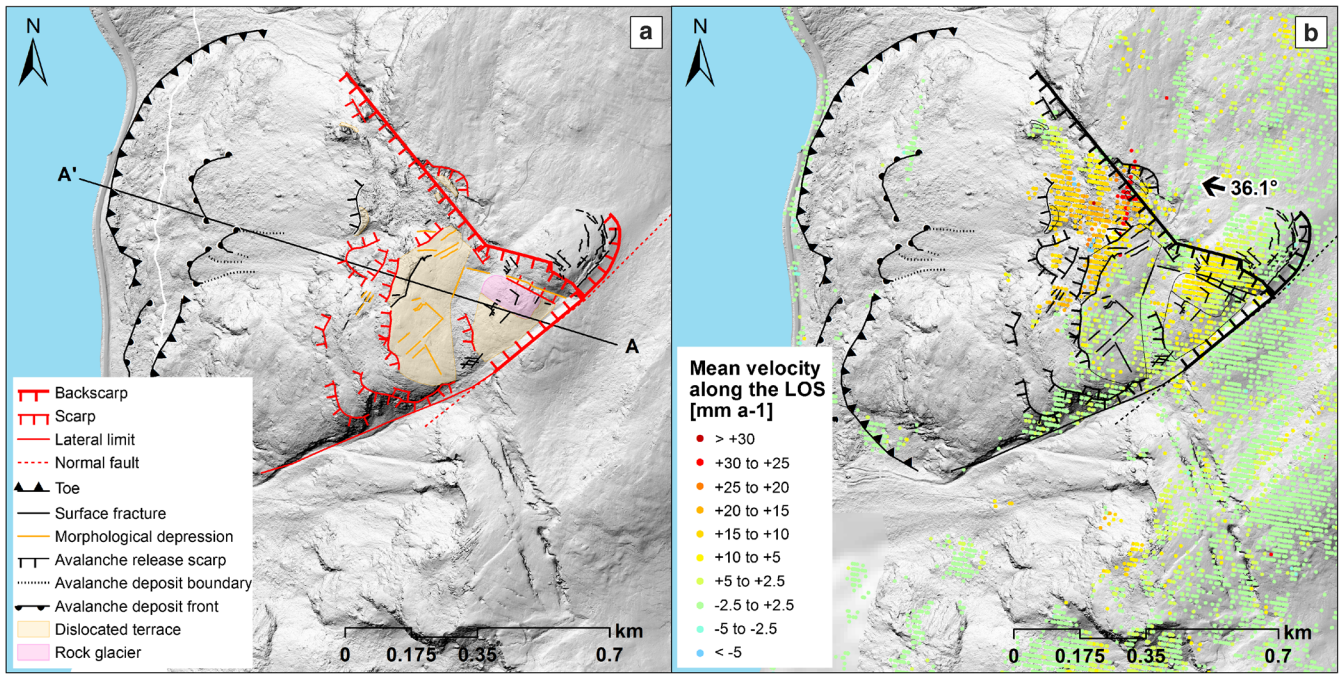
Fig. 22 **a** Morphostructure and location of A–A' profile. **b** InSAR mean velocity [mm/year] along line-of-sight (LOS) in descending geometry (orientation of black arrow: LOS azimuth angle, label: LOS incidence angle; NGU 2019b). Background: hillshade based on 0.5 m ALS-derived digital elevation model
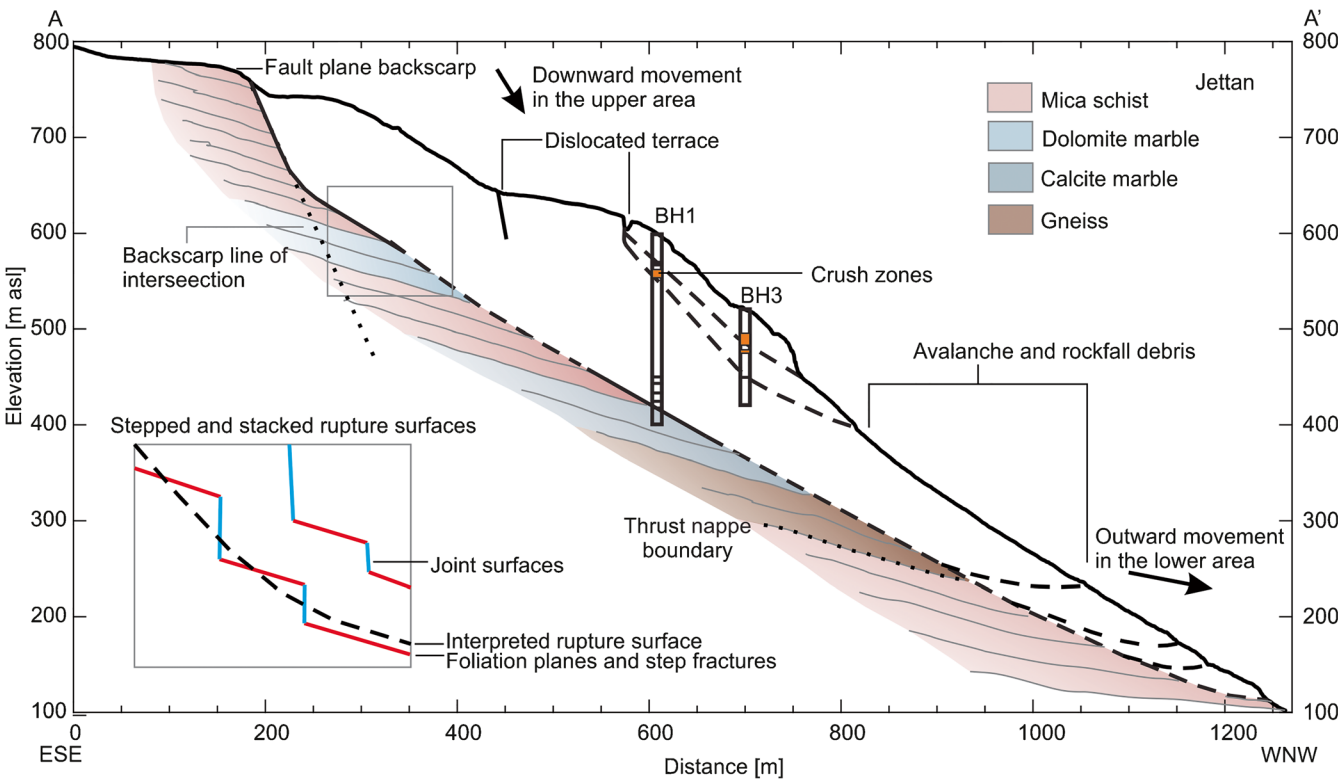
Fig. 23 A–A' cross section of Jettan, based on 0.5 m DEM (location on Fig. 22), showing exposed fault in the backscarp. Mapped rupture planes indicated by heavy black lines, and inferred rupture planes indicated by a dashed line. Inset is showing structural configuration of the rupture plane. Subsurface crush zones from borehole data (Elvebakk 2013, 2014; Ganerød 2013a, b). Movement arrows depict average surface movement vector from 3D InSAR (Eriksen et al. 2017a). Geology from Zwaan et al. (2006)
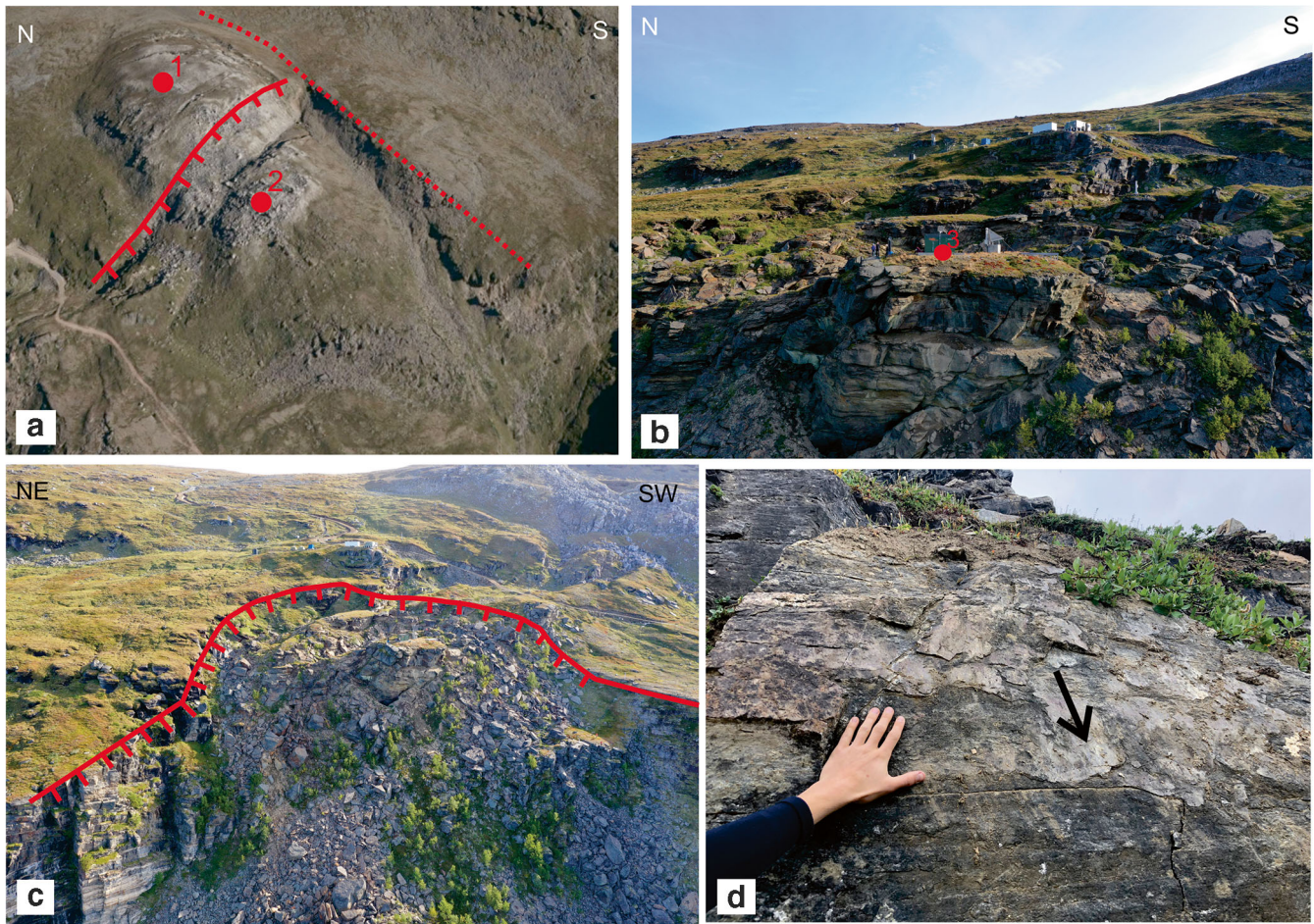
Fig. 24 **a** Apex of the backscarp intersection—a fault plane on the southern border bounds an offset in the lithology (mica schist in the southern scarp, metasediments on the northern scarp; www.norgeibilder.no) and intersects joint-controlled scarp on the N boundary. 1 indicates a marble dome sitting above the backscarp, 2 the active rock glacier (after Blikra and Christiansen 2014). **b** Stepped surface morphology of the RSD formed by a scarp-terrace assemblage (3. Location of borehole 2; Vick 2019). **c** Dislocated material/block field in the northern section of the RSD (outlined by red scarp) indicates some previous activity here, which has created space for material above to move (Vick 2019). **d** Slickenlines in the coating of the fault plane (Vick 2019)

fractures. These align both parallel with and perpendicular to the slope direction, indicating extension downslope and laterally. To the SW, close to the fault lateral limit, the surface shows a chaotic disaggregated block field, with possible avalanche deposits below, indicating a higher degree of deformation with proximity to the fault.

The chaotic morphostructure geometry implies a complex basal rupture, or network of ruptures. Added to this, a variety of structures from multiple phases of local tectonic deformation are present, including crenulation cleavage, kink folds and their axial plane cleavage and reactivated quartz veins. All these structures are planes of weakness within the RSD and have been observed to be utilised for various rupture surfaces in different locations. The joint sets generally crosscut these other minor structures indicating they are well developed and preferential rupture paths. The presence of faulting has likely had a large effect on the RSD, not only structurally but on the strength of the surrounding rock mass.

The basal rupture surface is difficult to delineate and has been postulated based on the lack of observable surface deformation below the toe line (Fig. 26). It is unclear how much the rear rupture

adheres to fault splay 2, as the fault surface is much steeper than the postulated basal rupture surface. We propose that the rear rupture follows the locally steep (35° NW) foliation immediately below the exposure of fault scarp 2. The rear rupture must transfer to a basal rupture lower in the slope, and likely in part follows the gentle foliation there (10–20° NW).

InSAR mean velocity values range from negligible (< 2.5 mm a^{-1}) or low (2.5–5 mm a^{-1} along the LOS) in the north-western part to 15–25 mm a^{-1} in the south-eastern part. This tends to indicate progressive change of movement orientation, where the central and south-eastern is more aligned with the LOS (WNW). In addition, the largest movements are connected to ongoing surficial activity closest to the fault.

Áhkávátgáisi

Áhkávátgáisi (also referred to as Kjerringdalen) is located at the meeting point of Kjerringdalen and Manndalen, approximately opposite Gámanjunni-3 and on the edge of an elongated N–S-trending plateau. The slope falls from the crest of the plateau at 920 m asl at an average slope angle of 30°. The unstable area
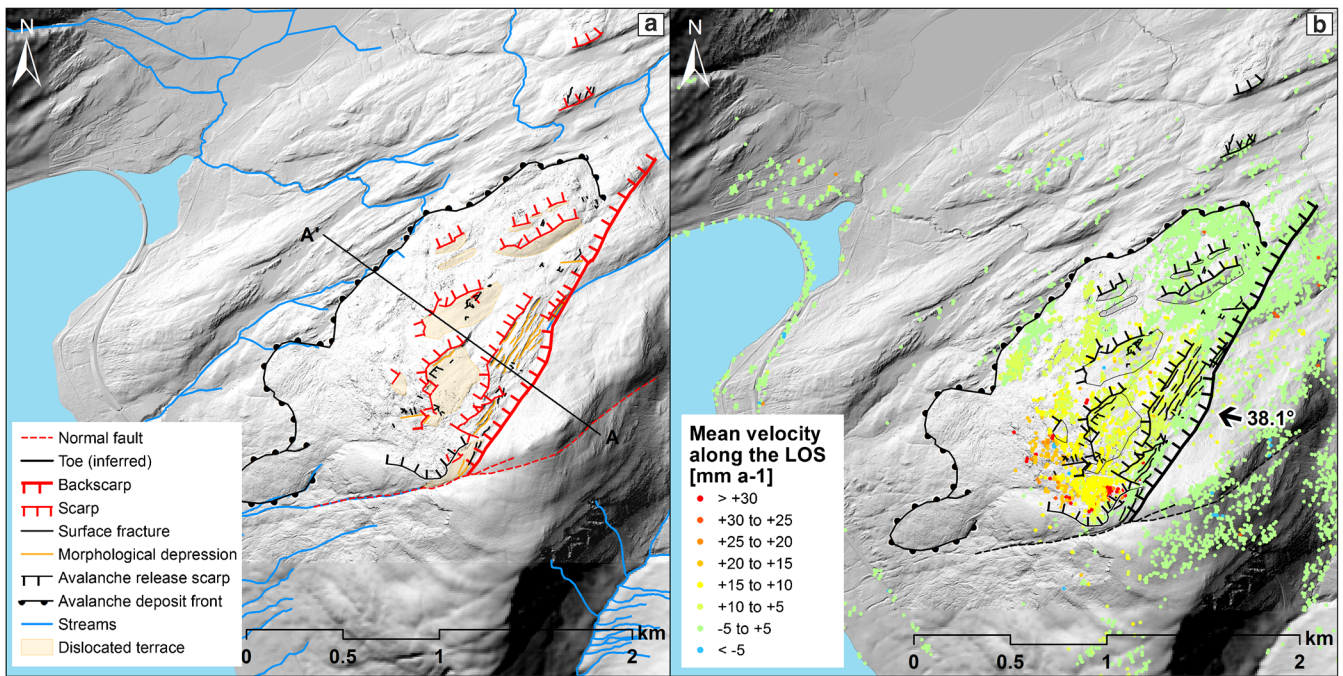
Fig. 25 **a** Morphostructure and location of A–A' profile. **b** InSAR mean velocity [mm/year] along line-of-sight (LOS) in descending geometry (orientation of black arrow: LOS azimuth angle, label: LOS incidence angle; NGU 2019b). Background: hillshade based on 0.5 m ALS-derived digital elevation model

consists of Kåfjord Nappe mica schists with varying amounts of biotite and muscovite, and calcareous schist of the Váddás Nappe below (Quenardel and Zwaan 2008). Foliation dips at an average of 10° to WSW.

The plateau is offset by the Kjerringdalen Fault, which crosscuts the mountain dipping NW. The fault aligns with other lineaments mapped in the local area thought to be faults, including the fault mapped at Jettan (Fig. 1; Quenardel and Zwaan 2008). The
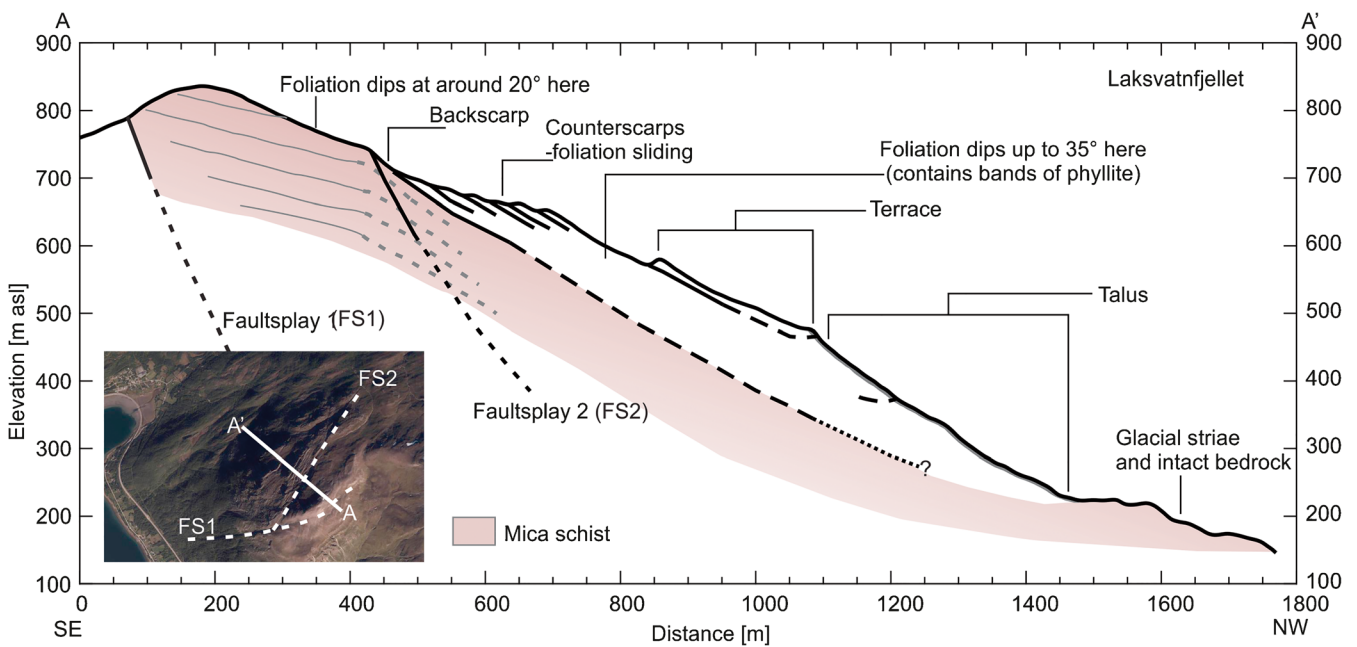
Fig. 26 A–A' cross section of Laksvatnfjellet, based on 0.5 m DEM (location on Fig. 25), showing exposed fault in the backscarp. Mapped rupture planes indicated by heavy black lines, and inferred rupture planes indicated by a dashed line. Basal rupture surfaces postulated (dotted line). Fault traces after Davids et al. (2013) and Rasmussen (2011). Geology from Zwaan et al. (1998)
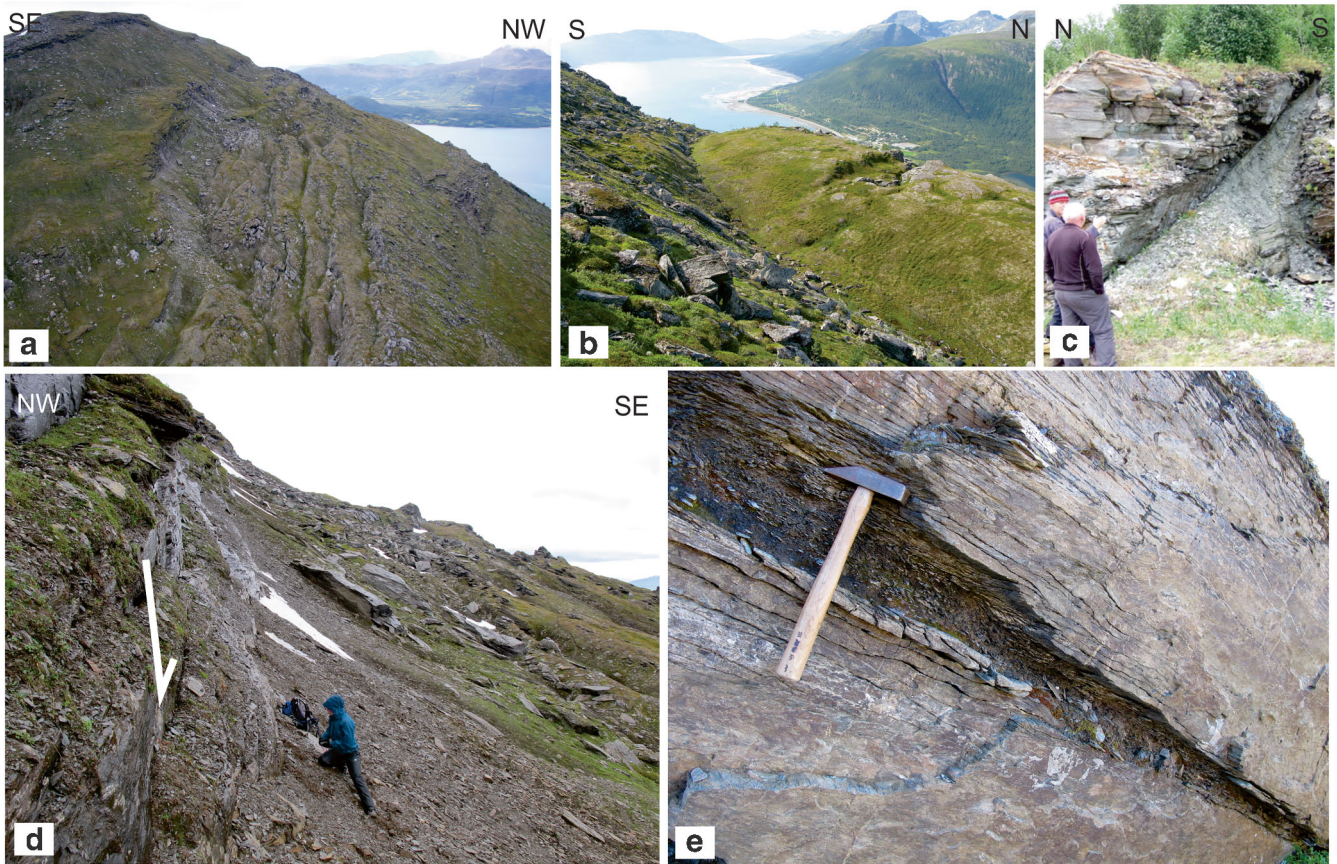
Fig. 27 a Counterscarps sliding on overturned foliation surfaces (Henderson 2007). b Backwards rotation of a dislocated terrace. Note the transverse fractures in the terrace surface providing a lateral spread of the terrace (Bergh 2010). c Fault plane outcropping in the lower W limit of the RSD, showing gouge (Rasmussen 2010). d Fault plane backscarp (Bergh 2010). e Layers of weaker phyllite within the surrounding schist (Bergh 2010)

Kjerringdalen Fault is normal and contains thick gouge and epidote mineralisation with movement indicators (Böhme et al. 2016a; Bunkholt et al. 2013c). The fault scarp clearly forms the backscarp of the RSD (Figs. 28 and 29), with little offset of the plateau at the NE end of the fault and increasing towards SW up to 40 m (Fig. 30a–c). The terraces display evidence of lateral spreading, as it is segmented by structures striking approximately perpendicular to the slope direction. At the SW end, the largest displacing block (see Fig. 30a) has moved as a coherent mass with an intact surface and appears to be sliding downwards and to the SW. The central terraces are following suit; however, they show less dislocation. In the NE area, a freestanding column contains a terrace which shows no dislocation (Fig. 30d). However, there is deformation observed within the upper column and the limit of this has been delineated (Figs. 28 and 30d).

The morphostructure becomes difficult to constrain below the dislocated. At the N side, most of the slope is outcropping in situ bedrock, which displays no clear sign of deformation (Figs. 28 and 30a). Deposits from a series of rock avalanche events cover the entire flank at the SW lateral limit. The avalanche deposits may be degraded from fluvial erosion at river level.

A toe has not been inferred due to a lack of morphostructural and morphological evidence. However, it is likely that there is load transfer to the shallow (10° dip) foliation lower in the slope, and

therefore, a basal rupture surface has been indicated to follow foliation (Fig. 29).

InSAR LOS orientation is well aligned with the slope. Results highlight velocities at around 6 mm a^{-1} along the LOS on the upper terrace. Higher velocities up to > 30 mm a^{-1} detected lower on the slope are attributed to superficial displacements in the rock avalanche deposits.

Discussion

The nature, geological and climatic history and lithological conditions of the Troms Mountains have created an environment in which slopes are able to respond to gravitational forcing by means of deformation. Precipitous slopes comprised of anisotropic rock mass provide a metastable environment (Bunkholt et al. 2012). Varying stress regimes from numerous glacial advance and retreat cycles, warm periods of intense precipitation and seismic activity have added to the cumulative slope damage and conditioned the slopes for failure (e.g. Böhme et al. 2019; Jarman 2004, 2009).

Regardless of the various environmentally conditioning factors that prime a slope for failure, the structure of the bedrock is considered the key factor controlling the exact location, failure mechanism and volume of the rockslides (Jaboyedoff et al. 2011; Stead and Wolter 2015). The sites discussed here are categorised according to which structural weakness is utilised
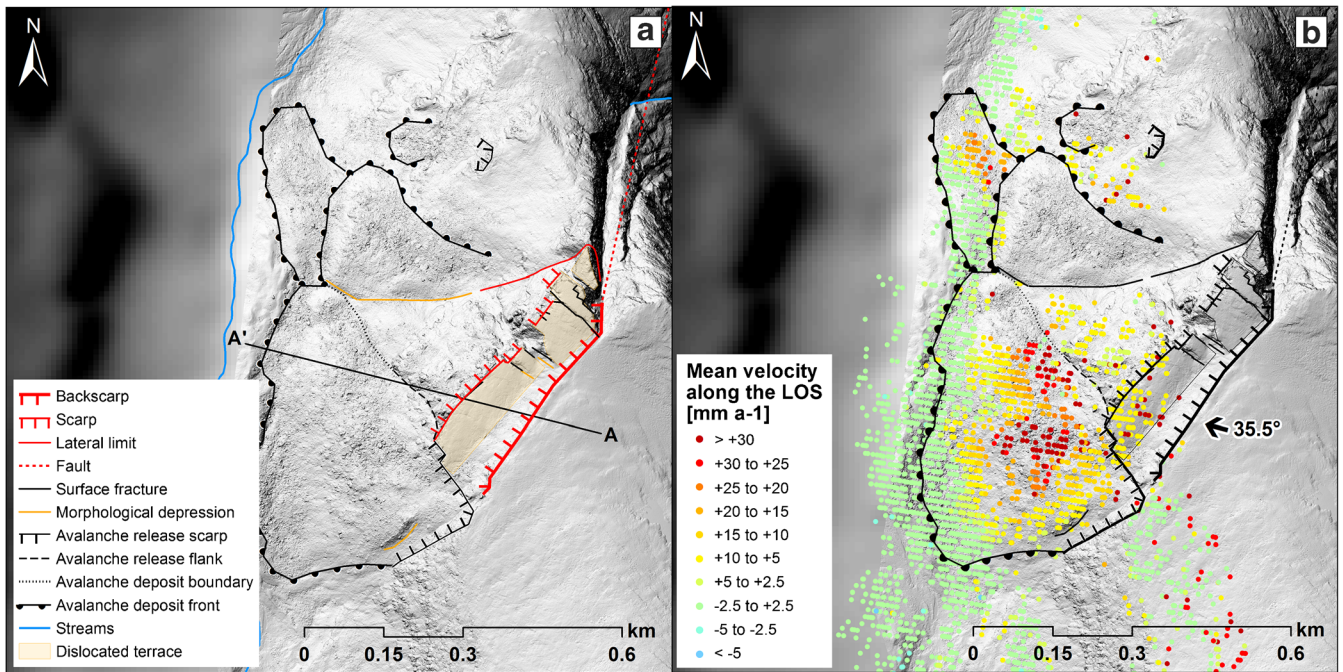
Fig. 28 **a** Morphostructure and location of A–A' profile. **b** InSAR mean velocity [mm/year] along line-of-sight (LOS) in descending geometry (orientation of black arrow: LOS azimuth angle, label: LOS incidence angle; NGU 2019b). Background: hillshade based on 0.5 m ALS-derived digital elevation model

for development of the rear rupture surface. This is not because we consider the rear rupture to be the most important, but rather that it is largely the only structure that is exposed and, in situ, as subsurface data are not yet available for all sites.

As no sites in this review can be classified as simple translational slides (e.g. sliding on one rupture surface), we discuss the sites within the framework of compound rockslides (after Glastonbury and Fell 2010). Compound rockslides utilise more than one surface type for rupture in order to daylight. The key
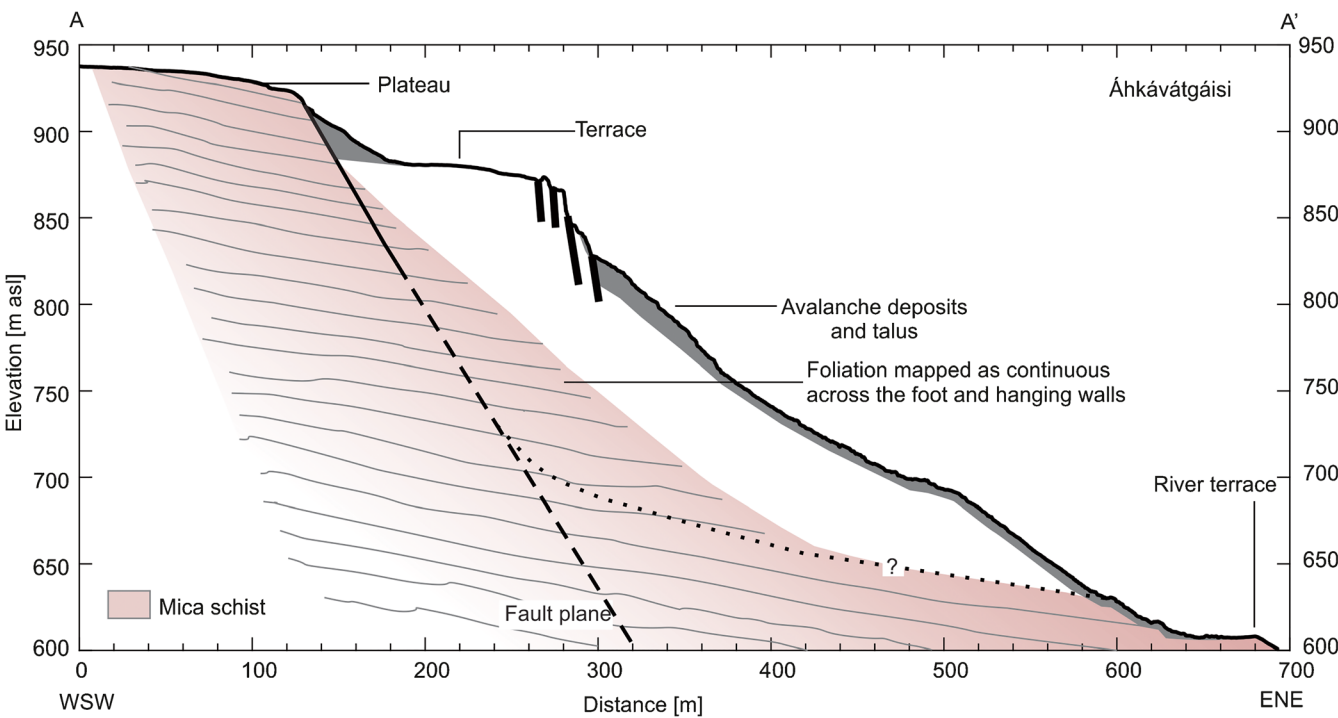
Fig. 29 A–A' cross section of Áhkávátgáisi, based on 0.5 m DEM (location on Fig. 28), showing exposed fault plane in the backscarp. Mapped rupture planes indicated by heavy black lines, and inferred rupture planes indicated by a dashed line. Fault trace after Bunkholt et al. (2013a). Geology from Quenardel and Zwaan (2008)
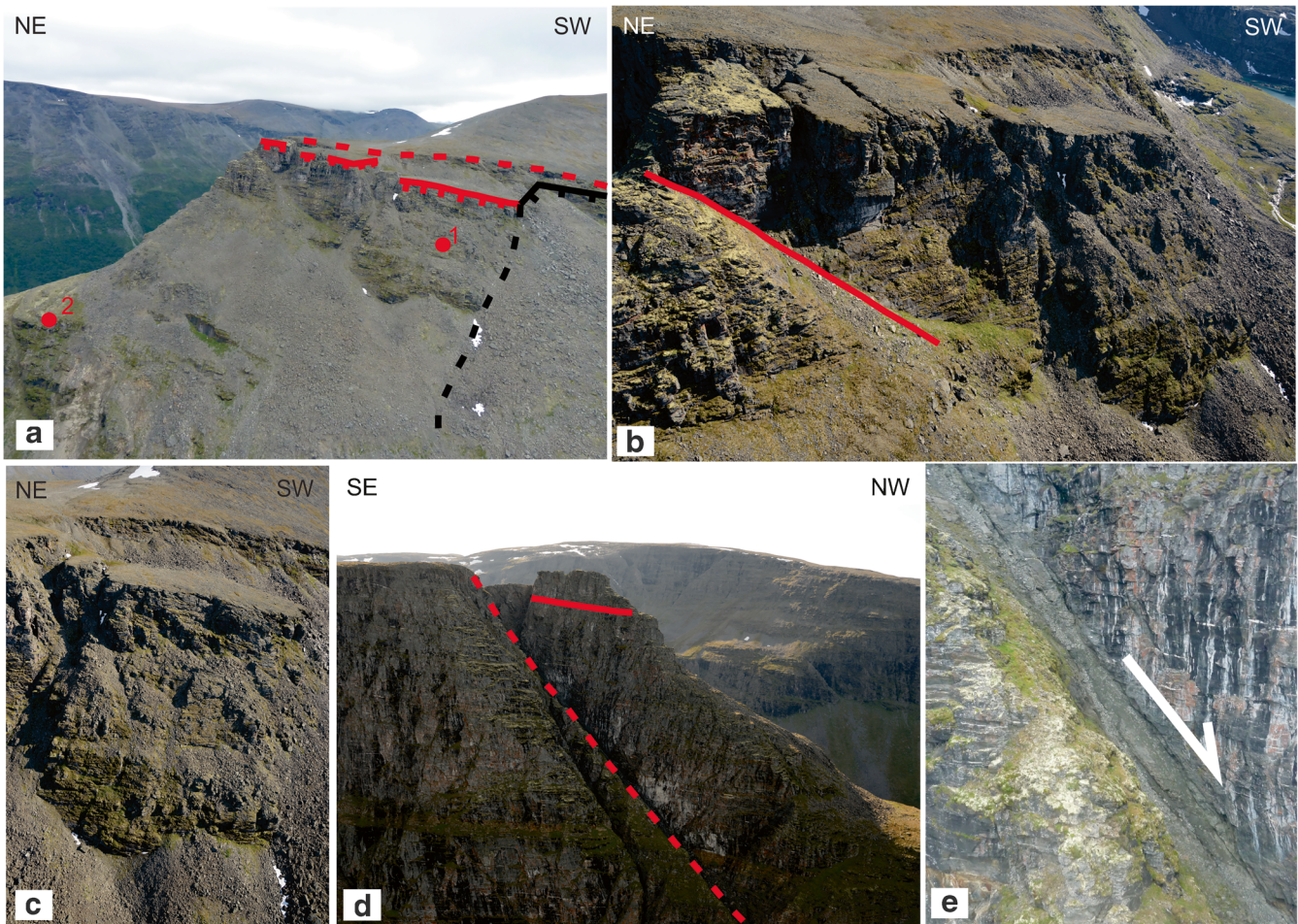
Fig. 30 a Overview image of the RSD indicating fault plane (red dashed line) and displacing blocks (Bunkholt 2011). 1. Main terrace block, with increased subsidence to the SW end. 2. Intact bedrock. **b** Terraces at the NE end show signs of subsidence and sliding to the S at the SW end. Lateral limit of deformation indicated by a red line (Bunkholt 2011). **c** The large displacing block in front view. **d** Exposure of the Kjerringdalen Fault as seen from the W. Note the lateral limit indicated in **b** extends to this side of the column (Böhme 2019). **e** Closer inspection of the fault gouge material (Böhme 2019)

characteristic of these being a basal sliding on a low-angle basal rupture surface, driven by the force of upper material being displaced along the rear rupture surface (Fig. 31). Loading from the active wedge (material at the head under tension) drives the passive wedge (material near the toe, under compression), which means sliding can be accommodated by low-angle surfaces. Typically shear planes near the toe of a compound slide display a friction angle that is higher than the inclination angle of the plane (Glastonbury and Fell 2010; Fig. 31a). High stress concentrations at the toe enable fracture propagation and coalescence for the formation of a consistent shear surface (e.g. Bolla and Paronuzzi 2017). We present an overview of key characteristics of each RSD in Table 1 and discuss and present an updated geotechnical schematic model for the three proposed rupture categories (Figs. 32 and 33).

Relevance of structure to the RSD development

The sites discussed in this review are a result of the unique structural environment in Troms: low to moderately dipping well-developed foliation, usually in highly anisotropic rock; ubiquitous steeply dipping joint sets; and inherited weakness zones such as faults. The medium- to high-grade metamorphic rocks span lithologies from meta-arkose to the ultramafic, the dominant lithologies being mica schists and gabbros (Zwaan 1988). The cluster of slope instabilities in the mapping area of this study of Troms (Fig. 1) has been largely attributed to the lithology (Bunkholt et al. 2012). These slopes are dominated by metasediments rather than metavolcanics, which are seen elsewhere in the region (Zwaan 1988; Zwaan et al. 1998). The former are known to have both a lower intact strength and friction angle than their igneous counterparts (e.g. Mair am Tinkhof et al. 2010). Both the lower competency of the lithology and the anisotropy of the foliated metamorphic rock masses prime the slopes for failure. Of particular note is the consistent occurrence of mica schist, a highly anisotropic rock which presents a geotechnical challenge to slope stability (Zhang et al. 2017). Mica schist is the dominant lithology in many notable mountain landslides around the world (e.g. Macfarlane 2009; Malone et al. 2008) and in Norway (e.g. Saintot et al. 2011). The anisotropic nature of schist means that the

rock is strongest when foliation is dipping at 0 or 90°, and displays its lowest strength when dipping between 20 and 40° (e.g. Zhang et al. 2017). In the context of the Troms Mountains, foliation dip is dominantly shallow as a result of the imbricated nature of the thrust nappes which formed the fabric of the rock (Faber 2017). It is rare to see dip greater than 40° (Zwaan 1988). The thrust belt architecture has resulted in a foliation which dips dominantly between NW and SW (e.g. Augland et al. 2014). Foliation dip parallel with the slope occurs on NW, W and SW slope aspects, varying locally depending on the local structure. In these scenarios, the propensity of the rear rupture surface to align with foliation structure depends on the dip angle of the foliation. At sites where foliation is not dipping optimally for sliding, i.e. dipping at $\leq 20°$ with the slope, or into the slope, we observe rear rupture along a different structure than foliation.

The tectonic regime in Troms during rifting has resulted in three dominant discontinuity strikes—varying around NNE–SSW, NE–SW and NW–SE throughout the region (e.g. Bergh et al. 2007; Indrevær et al. 2013, 2014; Indrevær and Bergh 2014). The structures are mapped on a local scale at most sites. They are steep and oscillate in dip direction. Additionally, other local joint sets are sometimes mapped at the sites. These joint sets are consistently mapped as the rear rupture surface at sites where foliation dip is too shallow for backscarp rupture and where there is no fault present. Usually more than one joint set forms a backscarp. The joint patterns in Troms are controlled by the larger network of faults crosscutting the region. The lineaments crosscutting our specific mapping area display a dominant trend in the NE–SW direction (Fig. 2; Skrede 2013; Zwaan 1988b). Most NE–SW-striking faults are identified as inherited rift-era faults with gouge dated to the Permian at Laksvatnfjellet (Davids et al. 2013). Reactivated faults in this study are distinguished from gravity-induced rupture surfaces by the presence of old gouge (e.g. Laksvatnfjellet; Davids et al. 2013; Fig. 27), hydrothermal surface deposits (e.g. epidote at Áhkávátgáisi; Böhme et al. 2016a) and fibre lineations that show multiple phases of movement (e.g. Laksvatnfjellet; Rasmussen 2011). Of course, active

tectonics may play a role in the future at these sites. The catastrophic Tjelle rockslide in 1765 in western Norway was released on an inherited fault (Redfield and Osmundsen 2009), and the authors speculate that an earthquake may have triggered the collapse. However, due to the lack of information regarding neotectonic activity in the Troms region, the influence of active faulting on the RSDs can be acknowledged (Hermanns and Longva 2012) but not discussed.

The nature and geometry of the faults will control the deformation and failure mechanism of the RSDs (Martino et al. 2004). In this study, the faults act directly as a shear surface bounding a portion of the slide. In other cases, they may not specifically form the rear of basal sliding surface. For example, in the case of the La Clapière rockslide, French Alps, faults with associated gouge and crushed rock are reactivated to accommodate internal deformation (El Bedoui et al. 2011). The role of the inherited faults in the stability of the slopes presented here is clear: where sites on a NW-facing slope are proximal to a fault plane, the plane acts as a detachment surface. The fault planes are steeply dipping, and sliding is aided by the low shear strength of the gouge material. It is likely the surrounding bedrock has experienced hydrothermal fluid flow leading to a weakening in the intact rock strength and in the shear strength of localised discontinuities, further aiding deformation. Apart from acting as a shear surface, inherited faults may affect slope stability due to general tectonic damage and lowering of rock mass properties in the vicinity (e.g. Brideau et al. 2009; Hermanns and Longva 2012; Stead and Wolter 2015). Inventory studies show proximity to a fault increases the likelihood of RSD occurrence. For example, in Vietnam (Lee and Dan 2005) and Argentina (Hermanns and Strecker 1999), clusters of failures or deforming slopes are identified at or within the buffer zone of tectonic lineaments. At Laksvatnfjellet, many structures associated with local tectonics are mapped including crenulation cleavage, kink folds and their axial plane cleavage and reactivated quartz veins. The frequency of these structures in the rock mass act to both facilitate kinematic release and sliding, as well as to lower the overall rock mass properties.
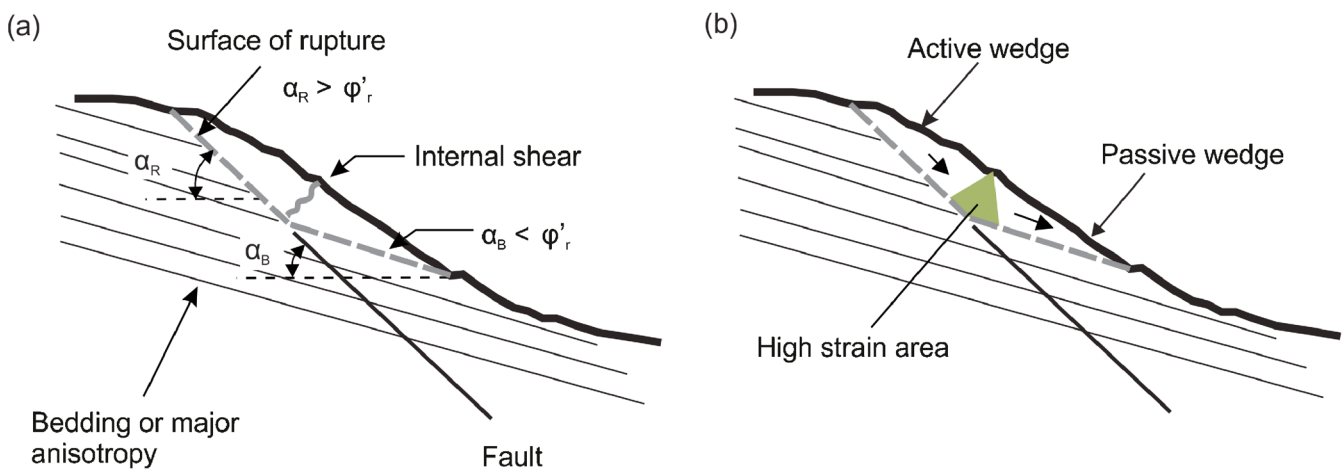
Fig. 31 a Geotechnical characteristics of a (simplified) compound slide, where surface of rupture comprises a rear surface inclination (α_R) higher than the residual friction angle (ϕ'_r), and a basal surface (α_B) which inclination is lower than the friction angle (ϕ'_r) of the basal surface. Transformation between the upper active portion and the lower passive portion results in internal shearing. After Glastonbury and Fell (2010). **b** A compound slide showing transition zone as a high strain area (after Stead and Wolter (2015), modified from Glastonbury and Fell (2010))

Table 1 Summary of characteristics for the nine RSDs described in this study

	Rear rupture surface	Dip of rear rupture surface	Mountain peak height [m asl]	Average slope angle [°]	Slope aspect	Average foliation dip [°]	Foliaiton dip direction
Nomedalstinden	Foliaiton	37.5	1051	20	SW	37.5	SW
Rismmalčohkka	Foliaiton	36	1096	20	SW	36	SW
Badjánanvárri	Foliaiton	35	1169	20	SW	35	SW
Gamanjunni-3	Joint intersection	45	1217	35	WSW	13	WNW
Váráš	Joints	Vertical	875	30	SW	20	SW
Oksfjellet	Joints	Vertical	1115	35	NE	27.5	NW
Jettan	Fault	65	861	35	W	17	NW
Laksvatnfjellet	Fault	65	876	25	NW	15	NW
Áhkávátgáisi	Fault	60	950	30	NW	13	NW

|	Joint strike orientations	Geology	Fault	Morphologically clear toe?	Proximity to thrust nappe boundary [km]
Nomedalstinden	E–W, NE–SW and NW–SE	Mica schist, meta-arkose, quartzite	–	✓	> 10
Rismmalčohkka	WNW–ESE and NE–SW	Mica schist, meta-arkose, quartzite	–	x	> 6
Badjánanvárri	E–W and NNE–SSW	Mica schist, meta-arkose, quartzite	–	x	> 5
Gamanjunni-3	WNW–ESE and NE–SW	Mica schist	–	✓	< 1
Váráš	NW–SE, NNE–SSW	Amphibolite, gneiss, mica schist, metasediments	–	✓	0
Oksfjellet	NNE–SSW, NE–SW and NW–SE	Mica schist	–	✓ (from displacement data only)	0
Jettan	NW–SE and SW–NE	Mica schist, marble	Normal, 65° to NW	✓	0
Laksvatnfjellet	NE–SW, NW–SE, N–S with large variance	Mica schist (presence of chlorite), lenses of amphibolite	Normal, 65° to NW	x	> 10
Áhkávátgáisi	NE–SW, NW–SE and N–S	Mica schist	Normal, 60° to NW	x	< 1
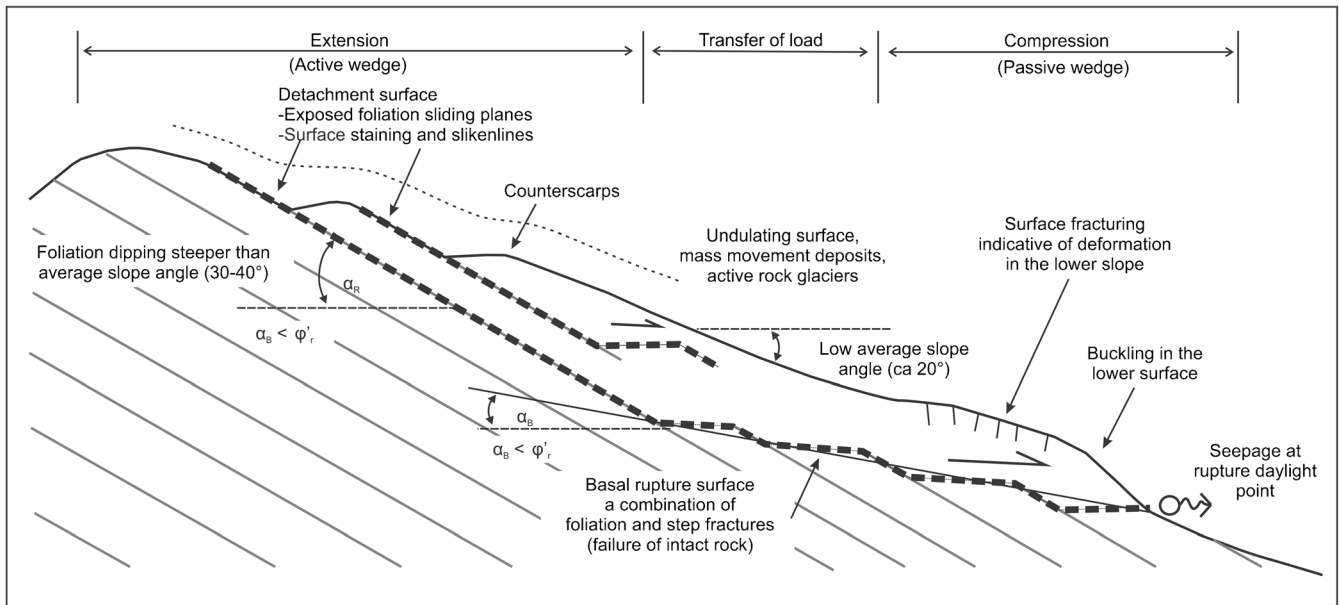
Fig. 32 Geomorphological and geotechnical schematic of foliation sliding

It is clear that these factors have predisposed the rock of Laksvatnfjellet to failure. However, it is not possible to determine if a RSD would exist in the same locations, if a fault did not. The dominance of the fault as the formative structure leading to the onset of deformation is difficult to ascertain.

The Caledonian nappes are separated by large thrusts which can be traced through the region (Zwaan 1988; Zwaan et al. 1998).

The exact role of these thrusts on the stability of the slopes is unknown. The resultant damage state of the rock mass at and surrounding the thrust zone is unlikely to have been preserved, as thrusting occurred in the Devonian–Silurian (Corfu et al. 2014) with multiple ductile deformation events occurring post emplacement. The idea that bedrock may be weakened proximal to thrust nappe boundaries should be explored in the context of these rock
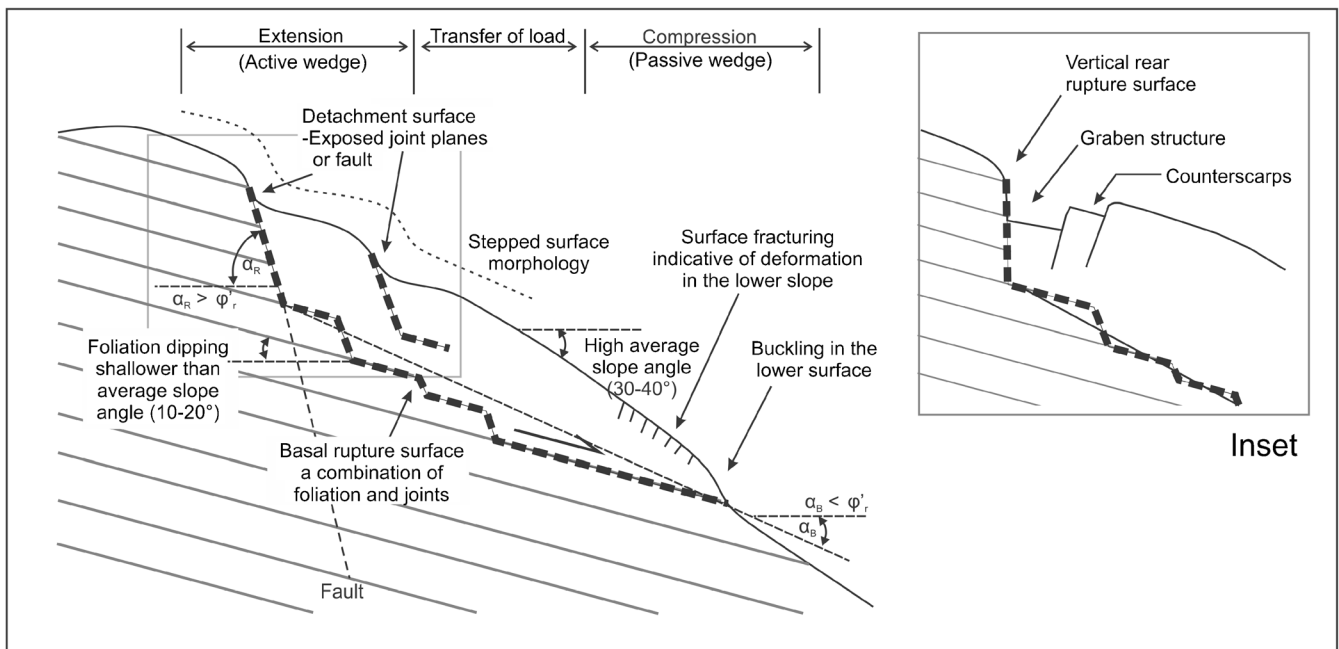
Fig. 33 Geomorphological and geotechnical schematic of joint and fault rupture RSDs. Inset shows a variation of the same whereby the rear rupture is steep enough to allow a formation of a graben structure below the backscarp

slope instabilities. Reports of nappe structures controlling the development of RSDs in other mountainous regions report associated lithological conditions as the reason for increased instability in the proximity of the nappes. For example, in the Carpathians, the landslide inventory shows a positive association between landslide occurrence and thrust nappe boundaries, highest within 75 m of the mapped boundary (Neuhäuser et al. 2012). Lithological boundaries between sandstone and weaker layers of claystone associated with nappe structures are thought to control the development of these large deep-seated RSDs (Chalupa et al. 2018). Agliardi et al. (2009) theorise that a very large RSD in the Italian Alps is controlled at the basal sliding surface by a large shear zone represented the nappe boundary. Other studies recognise the control nappe boundaries have with local deep-seated RSDs (e.g. Ambrosi and Crosta 2006). Nappe boundaries in Troms generally represent a change in lithology and metamorphic grade. The rocks are pervasively sheared making boundaries difficult to distinguish as they are not obviously higher strain zones relative to the nappe interiors (Faber 2017). However, the nappe boundaries or associated intra-nappe thrusts may represent a behavioural change and a structural weakness as they stand in present day. Tectonic structures can act as both kinematic release planes and to lower the overall strength of the entire rock mass (Brideau et al. 2009).

This is especially relevant as many of the sites in this review contain or are proximal to a nappe boundary within the mountain slope profile and, in the case of Oksfjellet, are utilising it for sliding. It is possible that the thrust boundaries or associated smaller thrusts have a lower shear strength, assisting sliding on the low-angle basal rupture surfaces of the RSDs.

Characteristics of foliation-controlled rear rupture RSDs

Based on the failure mechanism and characteristics of the Nomedalstinden, Rismmalčohkka and Badjánanvárri RSDs, we present a geotechnical schematic model for foliation-controlled rear rupture (Fig. 32). Nomedalstinden, Rismmalčohkka and Badjánanvárri are large foliation rupture examples, with deformation extending most of the length of the slope from crest to slope base. The slope surfaces are gently undulating, with an average slope dip of 20°, shallower than the foliation of 35–37.5°.

The key feature of these slides is the exceptionally clear rear rupture surface. Identification of foliation as the rear rupture surface is clear from foliation-parallel surfaces at the head of the RSD (Figs. 6 and 9). Multiple subsidiary scarps below the backscarp are also foliation-parallel. These bound sliding slabs of material, which have separated during sliding, rather than moving together as a coherent mass. The slabs form terraces at the head. The degree of horizontal extension is greater than at the other sites, due to the low angle of the rear rupture (relative to rear ruptures in this study which are near vertical). This has resulted in the gentle, undulating appearance of the slope surface. Surficial material fills space in the back of the terraces and lowers the surface waviness.

With the exception of Nomedalstinden, where foliation shallows towards the toe creating an ideal basal rupture surface, the rear rupture surface does not daylight at the slope base. The failure mechanism therefore must be compound, with the rupture surface utilising more than one surface type in order to daylight. We propose that the rupture surface transfers to a basal rupture surface in the central portion of the slope. Analogues and

mechanical models of compound slides dictate that internal shearing in the transfer zone will present as a higher degree of brittle fracturing in the transfer zone surface (Eberhardt et al. 2002; Glastonbury and Fell 2010; Stead and Eberhardt 2013). Therefore, the central slopes (300–700 m asl) are expected to show evidence of high strain. The sites presented here are generally talus covered and morphostructure is difficult to observe. However, there are sporadic preserved glacial geomorphic features in the lower reaches of this transfer zone, which indicate that the slope damage here is not as high as in the upper reaches.

The basal rupture surface of these slides is interpreted to be a combination of foliation, step fractures, other discontinuities and fracturing of intact rock. The high degree of extension seen at the head of the slope results in compressional forces at the toe. Compressive features mapped include buckling or bulging of the slope surface, and surface fracturing, which may also indicate thrusting. The presence of a daylighting basal rupture surface at the base of Nomedalstinden is supported by the hydrogeology—groundwater springs seep from the base of the toe area along a large position of the toe line.

InSAR detection of surface displacement at these sites is not ideal given the orientation of the slopes relative to the Sentinel-1 LOS down to the W. Only some portions of this movement can be detected. Within these limitations, a pattern can be derived (Figs. 4, 7 and 10). The rock glaciers show the highest rates of surface deformation within the LOS (10 to > 30 mm a^{-1}). Nomedalstinden and Rismmalčohkka show movement limited to the area between the highest and lowest counterscarps (10–20 mm a^{-1}), which is partially due to the lack of data lower on the slope where vegetation is denser.

Characteristics of joint- and fault- controlled rear rupture RSDs

Based on the failure mechanism and characteristics of the Gámanjunni-3, Váráš, Oksfjellet, Jettan, Laksvatnfjellet and Áhkávátgáisi RSDs, we present a geotechnical schematic model for joint and fault plane rupture RSD (Fig. 33). Similar characteristics apply to both joint and fault rupture RSD due to the steep nature of the rear rupture surface. These RSDs display a more constrained extent than RSDs of the former category, with steep slopes on average 30–40°.

Joint and fault surfaces at the rear are easily identified within or as the backscarp. Faults tend to be of a shallower dip (60–70°) than the joints, which are usually vertical or near vertical. In several cases, a combination of orthogonal backscarps (Gámanjunni-3 and Jettan) form a shallower intersection line plunge (45° and 65°, respectively) than the dip of its structural components. In these scenarios, where the detachment surface dips between 45 and 70°, the nature of the extension is shear. Where the detachment surface dips > 70° (Váráš and Oksfjellet), a tensile opening across the rear rupture is observed (Fig. 33 inset). This allows a relaxation of the unstable mass, forming a graben structure and subsequent counterscarps.

With no possibility for these high angled joints and faults to daylight within the slope surface, transfer to low-angled basal rupture surface is certain. However, the persistence of the rear rupture surface at depth is unknown, so pinpointing the transfer zone is difficult. The basal rupture surface likely follows foliation, with steps across joint surfaces. Foliation dips with the slope at 10–20° at all sites with the exception of Oksfjellet. Some steps on joints or step

fractures are likely. The daylighting of the basal rupture surface is inferred on the slope at all examples except Laksvatnfjellet and Áhkávátgáisi from evidence of surface damage, compression and thrusting in the lower slope. Gámanjunni-3 displays an exceptional example of a well-constrained basal limit—the rock in the lower portion has been thrust outwards, and evidence of fluid flow along the base of the slide indicates a preferential path for groundwater flow (Fig. 15). Generally, there is a lesser talus supply in the central and upper parts of the joint-controlled rear rupture sites than the other sites, implying there is less internal deformation occurring there. They all have considerable talus accumulation below the toe. This implies that where the rupture follows joint surfaces, they require very little propagation of shear surfaces through intact rock, and the failure requires very little internal deformation for release (e.g. Stead and Eberhardt 2013).

The bedrock at fault plane rupture RSDs shows a high degree of degradation, supplying talus to the slope through surficial processes and hinting at the advanced state of damage at these sites. Although they have similar failure mechanisms, while joint-controlled rear rupture examples move as a cohesive mass, the fault-controlled rear rupture examples display an unconstrained chaotic and blocky morphology that is difficult to interpret. Jettan, Laksvatnfjellet and Áhkávátgáisi are heavily segmented RSDs, with moving parts of varying sizes and geometries. This is likely the result of both the weakness of the bedrock from fault activity, the presence of multiple types of structures presenting many different planes of weakness available for deformation to utilise, and the complex geometry of back- and lateral-bounding structures as they interact with the fault structure.

Without further examples for comparison, it is difficult to say whether these slopes would be unstable if faults were not present. It is also difficult to say if foliation would be dominant over a fault, if both steeply dipping foliation and a fault were present in the same slope. More work is needed to understand the dominance of these RSDs.

In general, the joint and fault rear rupture examples show high surface deformation rates in areas which show evidence of surficial movement, e.g. > 30 mm a^{-1} across the avalanche deposits below scenario A at Váráš (Fig. 16), the rock glacier at Gámanjunni-3 (Fig. 13) or the disaggregated block field at Jettan (Fig. 22). The surface movement correlated to deep-seated deformation at joint-controlled rear rupture sites is well constrained by structural boundaries and is quite low at Váráš and Oksfjellet, whereas it is high at Gámanjunni-3. Displacement rates in bedrock are highest close to the fault rupture at Laksvatnfjellet, but higher away from the fault rupture at Jettan. Áhkávátgáisi is too small to make this differentiation. These irregularities make it difficult to determine a pattern in the kinematics for fault rupture RSDs.

Conclusions

Discontinuous rupture surfaces that form before catastrophic failure and during creep of RSD often follow pre-existing discontinuities in the bedrock. Understanding the development of the bounding rupture surfaces of a RSD allows for the assignment of a relevant failure mechanism and the quantification of potential failure volumes, key to characterising the slope hazard and risk. Rupture in the RSDs of Troms is observed to occur along repeating structural patterns determined by foliation angle, joint orientation and the presence of a fault. In shallow (ca 20°) slopes where

foliation dips steeply (30–40°) with the slope, foliation surfaces are utilised for rear rupture, termed here foliation-controlled rear rupture. Examples presented include Nomedalstinden, Rismmalčohkka and Badjánanvárri. These sites exhibit DSGSD morphology, with multiple terraces and large talus supply.

In slopes where foliation is shallow or where it dips in to the slope, joint planes have been utilised for rear rupture termed joint-controlled rear rupture. Examples of this presented are Gámanjunni-3, Váráš and Oksfjellet. These sites occur on steeper slopes and tend to move as a coherent block with less talus supply. Where inherited fault planes are present and dip parallel to the slope direction, they are utilised for rear rupture, termed fault-controlled rear rupture. Examples given include Jettan, Laksvatnfjellet and Áhkávátgáisi. They typically display chaotic morphostructure with a high talus supply.

As none of these rear rupture surfaces can daylight in the slope, we propose compound sliding, with a transfer of load to a shallow basal rupture surface. Evidence of compression and thrusting at the base of some of these slopes confirms that developed basal rupture surfaces are present, following low-angle surfaces such as shallow foliation in combination with step fractures or other structures. The different categories are morphologically distinct, and two simplified geotechnical and geomorphological models have been proposed to summarise them.

Data availability

All data sets presented are publically available for download at the referenced online locations, with the exception of maps from Figs. 4, 7, 10, 22, 25 and 28. These data will be made publically available in the near future by the Geological Survey of Norway.

Compliance with ethical standards

Conflict of interest The authors declare that they have no competing interests.

References

Agliardi F, Crosta G, Zanchi A (2001) Structural constraints on deep-seated slope deformation kinematics. Eng Geol 59:83–102. https://doi.org/10.1016/S0013-7952(00)00066-1

Agliardi F, Crosta GB, Frattini P (2012) Slow rock-slope deformation. In: Landslides. Types, mechanisms and modeling. Cambridge University Press, Cambridge, pp 207–221

Agliardi F, Crosta GB, Zanchi A, Ravazzi C (2009) Onset and timing of deep-seated gravitational slope deformations in the eastern Alps, Italy. Geomorphology 103:113–129. https://doi.org/10.1016/j.geomorph.2007.09.015

Ambrosi C, Crosta GB (2006) Large sackung along major tectonic features in the central Italian Alps. Eng Geol 83:183–200. https://doi.org/10.1016/j.enggeo.2005.06.031

Andresen A, Fareth E, Bergh SG, Kristensen SE, & Krogh E (1985) Review of Caledonian lithotectonic units in Troms, north Norway. In D. G. Gee & B. A. Sturt (Eds.), The Caledonide orogen: Scaninavia and related areas (pp. 570–578). Wiley

Augland LE, Andresen A, Gasser D, Steltenpohl MG (2014) Early Ordovician to Silurian evolution of exotic terranes in the scandinavian caledonides of the Ofoten-Troms area-terrane characterization and correlation based on new U-Pb zircon ages and Lu-Hf isotopic data. Geol Soc Spec Publ 390(1):655–678. https://doi.org/10.1144/SP390.19

Ballantyne CK (2002) Paraglacial geomorphology. Quat Sci Rev 21:1935–2017. https://doi.org/10.1016/S0277-3791(02)00005-7

Barboux C, Strozzi T, Delaloye R, Wegmüller U, Collet C (2015) Mapping slope movements in alpine environments using TerraSAR-X interferometric methods. ISPRS J Photogramm Remote Sens 109:178–192. https://doi.org/10.1016/j.isprsjprs.2015.09.010

Bergh SG, Eig K, Kløvjan OS et al (2007) The Lofoten-Vesterålen continental margin: a multiphase Mesozoic-Palaeogene rifted shelf as shown by offshore-onshore brittle fault-fracture analysis. Nor J Geol 87:29–58

Berthling I, Etzelmüller B (2011) The concept of cryo-conditioning in landscape evolution. Quat Res 75:378–384. https://doi.org/10.1016/j.yqres.2010.12.011

Blikra LH, Christiansen HH (2014) A field-based model of permafrost-controlled rockslide deformation in northern Norway. Geomorphology 208:34–49. https://doi.org/10.1016/j.geomorph.2013.11.014

Blikra LH, Eiken T, Henderson I, Venvik-Ganerød G (2006a) [Feasibility study of rockslides in Troms] Forprosjekt fjellskred i Troms – Status 2005. NGU Report 2006.040

Blikra LH, Henderson IHC, Nordvik T (2009) [Rockslide hazard at Nordnesfjellet in the Lyngenfjord, Troms] Faren for fjellskred fra Nordnesfjellet i Lyngenfjorden, Troms. NGU Report 2009.026

Blikra LH, Longva O (2009) Gravitational-slope features in Troms: indications of paleoseismic activity? NGU Report 2000:001

Blikra LH, Longva O, Braathen A et al (2006b) Rock slope failures in Norwegian Fjord areas: examples, spatial distribution and temporal pattern. Landslides Massive Rock Slope Fail:475–496. https://doi.org/10.1007/978-1-4020-4037-5_26

Bøe R, Longva O, Lepland A et al (2004) Postglacial mass movements and their causes in fjords and lakes in western Norway. Nor J Geol 84:35–55

Böhme M, Bunkholt H, Dehls JF, et al (2016a) [Geological model and hazard and risk classification of the unstable rock slope Gamanjunni 3 in Manndalen, Troms] Geologisk modell og fare- og risikoklassifisering av det ustabile fjellpartiet Gamanjunni 3 i Manndalen, Troms. NGU Report 2010.007

Böhme M, Bunkholt H, Oppikofer T et al (2016b) Using 2D InSAR data to understand the deformation mechanism of the unstable rock slope Gamanjunni 3, northern Norway. In: Aversa S, Cascini L, Picarelli L, Scavia C (eds) Landslides and engineered slopes. Experience, theory and practice. CRC, Rome, pp 443–449

Böhme M, Hermanns RL, Gosse J et al (2019) Comparison of monitoring data with paleo–slip rates: cosmogenic nuclide dating detects acceleration of a rockslide. Geology 47:1–4. https://doi.org/10.1130/G45684.1/4655152/g45684.pdf

Bolla A, Paronuzzi P (2017) Stress-strain modelling to investigate the internal damage of rock slopes with a bi-planar failure. In: Mikoš M, Vilímek V, Yin Y, Sassa K (eds) Advancing culture of living with landslides, Ljubljana, pp 397–405

Braathen A, Blikra LH, Berg SS, Karlsen F (2004) Rock-slope failures in Norway; type, geometry, deformation mechanisms and stability. Nor J Geol 84:67–88

Bredal M (2016) A structural, geomorphological and InSAR study of the unstable rock slope in Oksfjellet, Kåfjord, Troms. Dissertation, UiT The Arctic University of Norway

Brideau MA, Yan M, Stead D (2009) The role of tectonic damage and brittle rock fracture in the development of large rock slope failures. Geomorphology 103:30–49. https://doi.org/10.1016/j.geomorph.2008.04.010

Bunkholt H, Osmundsen PT, Redfield T, et al (2011) [ROS rockslides in Troms: status and analysis after fieldwork 2010] ROS fjellskred i Troms: status og analyser etter feltarbeid 2010. NGU Report 2011.031

Bunkholt H, Otterå S, Yugsi Molina FX, et al (2013a) [Investigation of unstable rock slopes in Troms - status and plans after fieldwork 2011 and 2012] Undersøkelser av ustabile fjellpartier i Troms – status og planer etter feltarbeid 2011 og 2012. NGU Report 2013.021

Bunkholt H, Redfield T, Oppikofer T et al (2013b) The role of inherited structures in deep seated slope failures in Kåfjorden, Norway. In: Margottini C, Canuti P, Sassa K (eds) Landslide science and practice. Springer, Berlin, pp 7–35

Bunkholt H, Redfield TF, Osmundsen PT et al (2012) Landslide processes in hard rock in Troms, Norway. In: Eberhardt E, Froese C, Turner K (eds) Landslides and Enginereed slopes. CRC, Canada, pp 855–861

Carlà T, Intrieri E, Raspini F, Bardi F, Farina P, Ferretti A, Colombo D, Novali F, Casagli N (2019) Perspectives on the prediction of catastrophic slope failures from satellite InSAR. Sci Rep 9:14137. https://doi.org/10.1038/s41598-019-50792-y

Chalupa V, Pánek T, Tábořík P, Klimeš J, Hartvich F, Grygar R (2018) Deep-seated gravitational slope deformations controlled by the structure of flysch nappe outliers: insights from large-scale electrical resistivity tomography survey and LiDAR mapping. Geomorphology 321:174–187. https://doi.org/10.1016/j.geomorph.2018.08.029

Chigira M (1992) Long-term gravitational deformation of rocks by mass rock creep. Eng Geol 32:157–184. https://doi.org/10.1016/0013-7952(92)90043-X

Corfu F, Andersen TB, Gasser D, Chew DM (2014) The Scandinavian Caledonides: main features, conceptual advances and critical questions. Geol Soc Lond Spec Publ 390:9–43. https://doi.org/10.1144/SP390.25

Corner GD (2005) Scandes Mountains. In: Seppälä M (ed) The physical geography of Fennoscandia. Oxford University Press, p 468

Cruden DM, Varnes DJ (1996) Landslide types and processes. Transportation Research Board special report

Davids C, Wemmer K, Zwingmann H, Kohlmann F, Jacobs J, Bergh SG (2013) K-Ar illite and apatite fission track constraints on brittle faulting and the evolution of the northern Norwegian passive margin. Tectonophysics 608:196–211. https://doi.org/10.1016/j.tecto.2013.09.035

Eberhardt E, Kaiser PK, Stead D (2002) Numerical analysis of progressive failure in natural rock slope. In: Dinis da Gama C, Ribeiro e Sousa L (eds) EUROCK 2002 – ISRM international symposium on rock engineering for mountainous regions. Funchal, Madeira, pp 145–153

Eckerstorfer M, Eriksen HØ, Rouyet L, Christiansen HH, Lauknes TR, Blikra LH (2018) Comparison of geomorphological field mapping and 2D-InSAR mapping of periglacial landscape activity at Nordnesfjellet, northern Norway. Earth Surf Process Landf 43:2147–2156. https://doi.org/10.1002/esp.4380

eKlima. Free access to weather- and climate data from Norwegian Meteorological Institute from historical data to real time observations. http://eklima.met.no. Accessed 19 Mar 2020

Eig, K (2008) Onshore and offshore tectonic evolution of the Lofoten passive margin, North Norway, PhD thesis, University of Tromsø, Tromsø, Norway, pp 256

Eig K, Bergh SG (2011) Late Cretaceous-Cenozoic fracturing in Lofoten. North Norway: Tectonic significance, fracture mechanisms and controlling factors, Tectonophysics 499:190–215

El Bedoui S, Bois T, Jomard H et al (2011) Paraglacial gravitational deformations in the SW Alps: a review of field investigations, 10Be cosmogenic dating and physical modelling. Geol Soc Spec Publ 351:11–25. https://doi.org/10.1144/SP351.2

Elvebakk H (2014) [Borehole logging with optical televiewer, Bh 2 and Bh 3, Jettan, Nordnesfjellet,Kåfjord Municipality, Troms] Borehullslogging med optisk televiewer, Bh 2 og Bh 3, Jettan, Nordnesfjellet, Kåfjord kommune, Troms, NGU Report 2014.016

Elvebakk H (2013) [Borehole logging with optical televiewer, Jettan 1, Nordnesfjellet, Kåfjord Municipality, Troms] Borehullslogging med optisk televiewer, Jettan 1, Nordnesfjellet, Kåfjord kommune, Troms. NGU Report 2013.020

Eriksen HØ (2017) Combining satellite and terrestrial interferometric radar data to investigate surface displacement in the Kåfjord area. Dissertation, UiT The Arctic University of Norway

Eriksen HØ, Bergh SG, Larsen Y et al (2017a) Relating 3D surface displacement from satellite- and ground-based InSAR to structures and geomorphology of the Jettan rockslide, northern Norway. Nor J Geol 97:233–253

Eriksen HØ, Lauknes TR, Larsen Y, Corner GD, Bergh SG, Dehls J, Kierulf HP (2017b) Visualizing and interpreting surface displacement patterns on unstable slopes using multi-geometry satellite SAR interferometry (2D InSAR). Remote Sens Environ 191:297–312. https://doi.org/10.1016/j.rse.2016.12.024

Faber C (2017) Mountain building processes in the northern Norwegian Caledonides. Dissertation, UiT The Arctic University of Norway

Ferretti A, Prati C, Rocca F (2000) Nonlinear subsidence rate estimation using permanent scatterers in differential SAR interferometry. IEEE Trans Geosci Remote Sens 38(5):2202–2212. https://doi.org/10.1109/36.868878

Ferretti A, Prati C, Rocca F (2001) Permanent scatterers in SAR interferometry. IEEE Trans Geosci Remote Sens 39(1):8–20. https://doi.org/10.1109/36.898661

Frattini P, Crosta GB, Rossini M, Allievi J (2018) Activity and kinematic behaviour of deep-seated landslides from PS-InSAR displacement rate measurements. Landslides 15:1053–1070. https://doi.org/10.1007/s10346-017-0940-6

Furseth A (2006) [Landslide accidents in Norway] Skredulykker i Norge. Forlag Tun

Ganerød G V (2013a) Geological logging of drill core from borehole NN-01-12 at Jettan, Nordnes mountain in Troms county, northern Norway. Report no 2013.042

Ganerød G V (2013b) Geological logging of drill core from borehole NN-01-12 at Jettan, Nordnes mountain in Troms county, northern Norway. NGU report 2013.042

Gee DG, Fossen H, Henriksen N, Higgins AK (2008) From the early Paleozoic platforms of Baltica and Laurentia to the Caledonide Orogen of Scandinavia and Greenland. Episodes 31(1):44–51. https://doi.org/10.18814/epiiugs/2008/v31i1/007

Glastonbury J, Fell R (2010) Geotechnical characteristics of large rapid rock slides. Can Geotech J 47:116–132. https://doi.org/10.1139/T09-080

Glimsdal S, Løvholt F (2018) Displacement wave from rock slope failure in Lyngen. Propogration assessment using probabilistic methods [in Norwegian: Flodbølger etter fjellskred i Lyngen. Oppskyllingsberegninger ved hjelp av probabilistiske metoder]

Hannus M (2011) Structural geometry and controlling factors for a rock slope failure area at Hompen/Váráš, Signaldalen, Troms, North Norway. Dissertation, UiT The Arctic University of Norway

Hansen JA, Bergh SG (2012) Origin and reactivation of fracture systems adjacent to the mid-norwegian continental margin on Hamarøya, North Norway: Use of digital geological mapping and morphotectonic lineament analysis. Norw J Geol 92(4):391–403

Hegstad SK (2014) Post-glacial sedimentary processes and slope instabilities off Nordnesfjellet, Lyngenfjorden, northern Norway. Dissertation, UiT The Arctic University of Norway

Henderson IHC, Lauknes TR, Osmundsen PT, Dehls J, Larsen Y, Redfield TF (2011) A structural, geomorphological and InSAR study of an active rock slope failure development. Geol Soc Lond Spec Publ 351:185–199. https://doi.org/10.1144/SP351.10

Henderson IHC, Osmundsen PT, Redfield TF (2010) [ROS rockslides in Troms: Status and plans 2010] ROS Fjellskred in Troms: Status og planer 2010. NGU report 2010.021

Henderson IHC, Saintot A (2011) Regional spatial variations in rockslide distribution from structural geology ranking: an example from Storfjorden, western Norway. Geol Soc Lond Spec Publ 351:79–95. https://doi.org/10.1144/SP351.4

Hermanns RL, Longva O (2012) Rapid rock-slope failures. In: Clague JJ (ed) Landslides: types, mechanisms and modelling. Cambridge University Press, pp 59–70

Hermanns RL, Redfield TF, Bunkholt H et al (2012) Cosmogenic nuclide dating of slow moving rockslides in Norway in order to assess long-term slide velocities. In: Eberhardt E, Froese C, Turner K, Leroueil S (eds) Landslides and engineered slopes: protecting society through improved understanding. CRC, Alberta, pp 849–854

Hermanns RL, Schleier M, Böhme M et al (2017) Rock-avalanche activity in W and S Norway peaks after the retreat of the Scandinavian ice sheet. In: Mikos M et al (eds) Advancing culture of living with landslides. Springer International, pp 331–338

Hermanns RL, Strecker MR (1999) Structural and lithological controls on large quaternary rock avalanches (sturzstroms) in arid northwestern Argentina. Geol Soc Am Bull 111:934–948. https://doi.org/10.1130/0016-7606(1999)111<0934

Hernes I (2014) [A rockslide at Indre Nordnes, Nordnesfjellet, Lyngen, Troms - inner bedrock structure, movement mechanism based on structural analysis and monitoring data] Fjellskred ved Indre Nordnes, Nordnesfjellet , Lyngen, Troms — Berggrunnens indre struktur og beve. Dissertation, UiT The Arctic University of Norway

Humair F, Pedrazzini A, Epard JL, Froese CR, Jaboyedoff M (2013) Structural characterization of turtle mountain anticline (Alberta, Canada) and impact on rock slope failure. Tectonophysics 605:133–148. https://doi.org/10.1016/j.tecto.2013.04.029

Hungr O, Leroueil S, Picarelli L (2014) The Varnes classification of landslide types, an update. Landslides 11:167–194. https://doi.org/10.1007/s10346-013-0436-y

Husby EH (2011) [A rockslide at Nomedalstinden: a structurally-controlled moving mass on an underlying large-scale sliding surface] Fjellskred i Nomedalstinden: En strukturstyrt masseutglidning på et underliggende storskala glideplan, Thesis, University of Tromsø, Tromsø. Dissertation, UiT The Arctic University of Norway

Indrevær K, Bergh SG (2014) Linking onshore-offshore basement rock architecture and brittle faults on the submerged strandflat along the SW Barents Sea margin, using high-resolution (5 × 5 m) bathymetry data. Nor J Geol 94:1–34

Indrevær K, Bergh SG, Koehl JB et al (2013) Post-Caledonian brittle fault zones on the hyperextended SW Barents Sea margin: new insights into onshore and offshore margin architecture. Nor J Geol 93:167–188

Indrevær K, Stunitz H, Bergh SG (2014) On Palaeozoic-Mesozoic brittle normal faults along the SW Barents Sea margin: fault processes and implications for basement permeability and margin evolution. J Geol Soc Lond 171:831–846. https://doi.org/10.1144/jgs2014-018

Jaboyedoff M, Couture R, Locat P (2009) Structural analysis of Turtle Mountain (Alberta) using digital elevation model: toward a progressive failure. Geomorphology 103:5–16. https://doi.org/10.1016/j.geomorph.2008.04.012

Jaboyedoff M, Crosta GB, Stead D (2011) Slope tectonics: a short introduction. Geol Soc Lond Spec Publ 351:1–10. https://doi.org/10.1144/SP351.1

Jarman D (2009) Paraglacial rock slope failure as an agent of glacial trough widening. Geol Soc Lond Spec Publ 320:103–131. https://doi.org/10.1144/SP320.8

Jarman D (2004) Rock slope failure and landscape evolution in the Caledonian Mountains - A case study from Abisko, northern Sweden. Geografiska Annaler 84A(3–4): 213–224. https://doi.org/10.1111/j.0435-3676.2002.00176.x

Kartverket (2019a) Høydedata. www.hoydedata.no/LaserInnsyn/. Accessed 17 Jun 2019

Kartverket (2019b) Norge i bilder. www.norgeibilder.no. Accessed 17 Jun 2019

Lauknes TR, Shanker AP, Dehls JF et al (2010) Detailed rockslide mapping in northern Norway with small baseline and persistent scatterer interferometric SAR time series methods. Remote Sens Environ 114:2097–2109

Koehl JBP, Bergh SG, Henningsen T, Inge Faleide J (2018) Middle to late Devonian-Carboniferous collapse basins on the Finnmark Platform and in the Southwesternmost Nordkapp basin, SW Barents Sea. Solid Earth 9(2):341–372. https://doi.org/10.5194/se-9-341-2018

Lee S, Dan NT (2005) Probabilistic landslide susceptibility mapping in the Lai Chau province of Vietnam: focus on the relationship between tectonic fractures and landslides. Environ Geol 48:778–787. https://doi.org/10.1007/s00254-005-0019-x

Lilleøren KS, Etzelmüller B (2011) A regional inventory of rock glaciers and ice-cored moraines in Norway. Geogr Ann Ser A Phys Geogr 93:175–191. https://doi.org/10.1111/j.1468-0459.2011.00430.x

Macfarlane DF (2009) Observations and predictions of the behaviour of large, slow-moving landslides in schist, Clyde dam reservoir, New Zealand. Eng Geol 109:5–15. https://doi.org/10.1016/j.enggeo.2009.02.005

Mair am Tinkhof K, Preh A, Tentschert E, et al (2010) FLAC 3D and adaptive Kalman-filtering – a new way to install effective alarm systems for landslides? In: Proceedings of the European rock mechanics symposium. Lausanne, Switzerland

Malone AW, Hansen A, Hencher SR, Fletcher CJN (2008) Post-failure movements of a large slow rock slide in schist near Pos Selim, Malaysia. In: Chen Z, Zhang J, Li Z et al (eds) Landslides and engineered slopes. CRC Taylor & Francis Group, London, pp 457–461

Martino S, Moscatelli M, Scarascia Mugnozza G (2004) Quaternary mass movements controlled by a structurally complex setting in the central Apennines (Italy). Eng Geol 72:33–55. https://doi.org/10.1016/j.enggeo.2003.06.005

Neuhäuser B, Terhorst B, Damm B (2012) Landslide identification and modelling in flysch areas of the European Alpine foreland. Z Geomorphol 56:115–146. https://doi.org/10.1127/0372-8854/2012/00119

NGU (2019a) Unstable rock slope inventory map. www.ngu.no. Accessed 29 Oct 2019

NGU (2019b) InSAR Norway. In: 14 Novemb. 2018. https://insar.ngu.no/. Accessed 15 Sep 2019

Nordvik T, Blikra LH, Nyrnes E, Derron MH (2010) Statistical analysis of seasonal displacements at the Nordnes rockslide, northern Norway. Eng Geol 114:228–237. https://doi.org/10.1016/j.enggeo.2010.04.019

NVE (2019) Rock avalanche monitoring. www.nve.no. Accessed 29 Oct 2019

Nystad TM (2015) [Stability analysis and modelling of the unstable rock slope Jettan at Nordnesfjellet, Troms] Stabilitetsanalyse og modellering av det ustabile fjellpartiet

Jettan på Nordnesfjellet, Troms. Dissertation, Norwegian University of Science and Technology

Olesen O, Blikra LH, Braathen A et al (2004) Neotectonic deformation in Norway and its implications: a review. Nor Geol Tidsskr 84:3–21

Olesen O, Bungum H, Dehls J et al (2013) Neotectonics, seismicity and contemporary stress field in Norway–mechanisms and implications. Quat Geol Norw 13:145–174

Oppikofer T, Hermanns RL, Sandøy G et al (2016) Quantification of casualties from potential rock-slope failures in Norway. Landslides Eng Slopes Exp Theory Pract:1537–1544. https://doi.org/10.1201/b21520-190

Osmundsen PT, Henderson IHC, Lauknes TR, Larsen Y, Redfield TF, Dehls J (2009) Active normal fault control on landscape and rock-slope failure in northern Norway. Geology 37:135–138. https://doi.org/10.1130/G25208A.1

Pánek T, Klimeš J (2016) Temporal behavior of deep-seated gravitational slope deformations: a review. Earth-Science Rev 156:14–38. https://doi.org/10.1016/j.earscirev.2016.02.007

Patton H, Hubbard A, Andreassen K, Auriac A, Whitehouse PL, Stroeven AP, Shackleton C, Winsborrow M, Heyman J, Hall AM (2017) Deglaciation of the Eurasian ice sheet complex. Quat Sci Rev 169:148–172. https://doi.org/10.1016/j.quascirev.2017.05.019

Pedrazzini A, Humair F, Jaboyedoff M, Tonini M (2016) Characterisation and spatial distribution of gravitational slope deformation in the upper Rhone catchment (western Swiss Alps). Landslides 13:259–277. https://doi.org/10.1007/s10346-015-0562-9

Penna IM, Böhme M, Hermanns RL et al (2017) Large-scale rockslope deformations in Sogn Og Fjordane County (Norway). In: Mikos M et al (eds) Advancing culture of living with landslides. Ljubljana, pp 601–606

Quenardel JM, Zwaan KB (2008) Bedrock geology map Manndalen 16331, 1:50 000. [In Norwegian: Beggrunnskart]

Radbruch-Hall DH (1978) Gravitational creep of rock masses on slopes. In: Voight B (ed) Rockslides and avalanches, 1: natural phenomena. Elsevier, Amsterdam, pp 607–657

Rasmussen E (2011) [The Laksvatnfjellet rockslide, Balsfjord, Troms; inner structure, morphology and sliding mechanism] Fjellskred i Laksvatnfjellet, Balsfjord, Troms; indre struktur, morfologi og skredmekanismer. Dissertation, UiT The Arctic University of Norway

Redfield TF, Osmundsen P T (2009) The Tjellefonna fault system of Western Norway: Linking late-Caledonian extension, post-Caledonian normal faulting, and tertiary rock column uplift with the landslide-generated tsunami event of 1756. Tectonophysics 474(1–2), 106–123. https://doi.org/10.1016/j.tecto.2009.02.006

Roberts D, Lippard SJ (2005) Inferred Mesozoic faulting in Finnmark: current status and offshore links. Norges Geologiske Undersøkelse Bulletin, 443(Dallmeyer 1988), 55–60. http://www.ngu.no/FileArchive/102/Bulletin443_5.pdf

Rønning JS, Dalsegg E, Heincke BH, et al (2008) [Geophysical measurements at Nordnesfjellet in the summer of 2007, Kåfjord Municipality, Troms] Geofysiske målinger på Nordnesfjellet sommeren 2007, Kåfjord kommune, Troms. NGU Report 2008.024. 33

Saintot A, Henderson IHC, Derron M-H (2011) Inheritance of ductile and brittle structures in the development of large rock slope instabilities: examples from western Norway. Geol Soc Lond Spec Publ 351:27–78. https://doi.org/10.1144/SP351.3

Schermer ER, fRedfield TF, Indrevaer K, Bergh SG (2017) Geomorphology and topography of relict surfaces: the influence of inherited crustal structure in the northern Scandinavian Mountains. J Geol Soc 174:93–109. https://doi.org/10.1144/jgs2016-034

Schlögel R, Malet JP, Doubre C, Lebourg T (2016) Structural control on the kinematics of the deep-seated La Clapière landslide revealed by L-band InSAR observations. Landslides 13:1005–1018. https://doi.org/10.1007/s10346-015-0623-0

Sikveland G (2019) A structural, geomorphological and InSAR study of the unstable rock slopes at Mellomfjellet, Nordreisa. Dissertation, UiT The Arctic University of Norway

Skrede I (2013) [Jettan, Nordnesfjellet, Kåfjord, Troms- inner geometry and structure, kinematics and controllign factors of an unstable mountain slope based on structural analysis, geomorphology and monitoring data] Jettan, Nordnesfjellet, Kåfjord, Troms-indre geometri. Dissertation, UiT The Arctic University of Norway

Stead D, Coggan JS, Elmo D, Yan M (2007) Modelling brittle fracture in rock slopes - experience gained and lessons learned. In: Potvin Y (ed) Proceedings of the 2007 international symposium on rock slope stability in open pit mining and civil engineering, Perth, pp 239–252

Stead D, Eberhardt E (2013) Understanding the mechanics of large landslides. Ital J Eng Geol Environ:85–112. https://doi.org/10.4408/IJEGE.2013-06.B-07

Stead D, Wolter A (2015) A critical review of rock slope failure mechanisms: the importance of structural geology. J Struct Geol 74:1–23. https://doi.org/10.1016/j.jsg.2015.02.002

Sullivan TD (2007) Hydromechanical coupling and pit slope movements. In: Potvin Y (ed) Proceedings of the 2007 international symposium on rock slope stability in open pit mining and civil engineering, Perth, pp 3–43

Tolgensbakk J, Sollid JL (1988) Kåfjord, kvatærgeologi og geomofologi 1:50 000, 1634 2 [Kåfjord quaternary and geomorphology]. Geogr Institutt, Univ I Oslo

Yerro A, Pinyol NM, Alonso EE (2016) Internal progressive failure in deep-seated landslides. Rock Mechanics and Rock Engineering 49(6):2317–2332. https://doi.org/10.1007/s00603-015-0888-6

Zhang X, Ngai L, Wong Y et al (2017) Engineering properties of quartz mica schist. Eng Geol 121:135–149. https://doi.org/10.1016/j.enggeo.2011.04.020

Zwaan KB (1988) Bedrock geology map Nordreisa- M 1:250 000 [In Norwegian: Berggrunnsgeologisk kart]. Geological Survey of Norway

Zwaan KB, Dangla P, Quenardel J. (2006) Bedrock geology map Kåfjord 16342, 1:50 000 [In Norwegian: Berggrunnskart]

Zwaan KB, Farseth E, Grogan P. (1998) Bedrock geology map Tromsø, M 1:250 000 [In Norwegian Bergrunnsgeologisk kart]. Geological Survey of Norway

L. M. Vick (✉) · **L. Rouyet** · **S. G. Bergh** · **G. D. Corner**
Department of Geosciences,
UiT The Arctic University of Norway,
Dramsveien 201, 9009, Tromsø, Norway
Email: louise.m.vick@uit.no

M. Böhme
Geological Survey of Norway,
Leiv Eirikssons vei 39, 7040, Trondheim, Norway

L. Rouyet
Arctic Geology Department,
The University Centre in Svalbard (UNIS),
P.O. Box 1569171, Longyearbyen, Norway

L. Rouyet · **T. R. Lauknes**
NORCE Norwegian Research Centre AS,
Siva Innovasjonssenter, Sykehusveien 21, 9019, Tromsø, Norway